Exact energy harvesting analysis of multimodal piezoelectric beams using the dynamic stiffness method

Xiang Liu [a, b, c, *] , Yu Wang [a, b, c] , Sondipon Adhikari [d] , Weixian Zhou [a, b, c]

[a] Key Laboratory of Traffic Safety on Track, Ministry of Education, School of Traffic & Transportation Engineering, Central South University, Changsha, China
[b] Joint International Research Laboratory of Key Technology for Rail Traffic Safety, Central South University, Changsha, China
[c] National & Local Joint Engineering Research Center of Safety Technology for Rail Vehicle, Central South University, Changsha, China
[d] James Watt School of Engineering, University of Glasgow, Glasgow G12 8QQ, UK

HIGHLIGHTS

- Dynamic stiffness is developed for multimodal energy harvesting piezoelectric beams.
- Modeling technique is sufficient general to complex piezoelectric beam assemblies.
- Electrically-induced stiffness/damping introduced to characterize piezoelectric effects.
- Wittrick–Williams algorithm used in eigenvalue computation for efficient modal tuning.
- Energy harvesting analysis for beams with three typical tip attachments and circuits.

ARTICLE INFO

ABSTRACT

Piezoelectric vibration energy harvesting holds great potential for converting ambient vibrations into electrical energy. Establishing a suitable theoretical model to predict the performance of piezoelectric harvesters under base excitation is essential. This paper proposes a dynamic stiffness (DS) modeling technique to predict the electromechanical coupling responses of piezoelectric beams. The modeling technique is sufficiently general to be applied to a wide range of simple cantilever or generally complex piezoelectric beam structures. For demonstration purposes, this technique is applied to model beams equipped with three typical tip attachments and connected to three representative external circuits, enabling a comprehensive multimodal analysis. The Wittrick–Williams (WW) algorithm is employed to efficiently calculate the eigenvalues of DS matrices with any desired accuracy. This aids in tuning the natural frequency of piezoelectric beams to match the ambient environmental vibration frequency. The concepts of electrically-induced stiffness and electrically-induced damping are introduced to characterize the impact of energy harvesting circuits on natural frequencies and output voltage of piezoelectric harvesters. Theoretical research specifically conducted on piezoelectric beams explores the effects of material parameters, structural dimensions, load resistance, and base excitation on vibration energy harvesting. Finite element simulation confirms that the proposed DS model, based on the exact solution of governing differential equations, can accurately and effectively predict the output performance of piezoelectric harvesters. The proposed method can emerge as a powerful tool for the design and optimization of piezoelectric energy harvesters.

1. Introduction

Vibration energy harvesting has emerged as a critical technology for converting mechanical vibrations from ambient environment into electrical energy. The harvested and converted energy finds diverse applications in powering ultra-low wireless sensors [1], structural health monitoring devices [2], wearable devices [3], implantable electronics [4], and Micro-Electro Mechanical Systems [5,6], effectively addressing power supply challenges. Generally, there are five energy conversion

mechanisms: electrostatic [7,8], electromagnetic [9,10], piezoelectric [11–13], magnetostrictive [14,15], and triboelectric [16–18] transducers, as well as hybrid energy harvesting [19,20] that includes two or more of the above methods. Among these mechanisms, piezoelectric converters perform exceptionally well due to their simple structure, infinite lifespan, lower resonant frequencies, and no need for additional driving power.

It is well known that the peak output voltage of piezoelectric energy harvesters always occurs at their resonance frequencies. To enhance harvesting efficiency and broaden resonant frequency bandwidth, various piezoelectric structures have been proposed and optimized, including T-shaped beams [21–23], L-shaped beams [24–26], tapered beams [27,28], and cantilever arrays [29–31]. In addition to modifying the harvesting structures, other approaches like elastic magnifiers and coupled impacted beams [32,33] can also be employed to achieve broadband energy harvesting capabilities. All of these optimized structures are developed based on the most common cantilevered piezoelectric beam [34–36], known for its ability to generate significant mechanical strain with vibrations. Researchers have developed substantial mathematical models [37–40] to predict the electromechanical coupling response of this cantilevered energy harvester under a given base excitation.

Umeda et al. [41] were among the pioneers in the study of piezoelectric transducers and introduced an equivalent circuit model (ECM) to simulate energy generation mechanism of piezoelectric oscillators. In a subsequent work [42], they conducted a study on energy storage characteristics of piezoelectric generators, providing a valuable reference for other scholars [43–45]. ECM simplified the harvesters as a single-degree-of-freedom (SDOF) system using a direct electromechanical analogy which was only applicable to specific generators and could not adapt to higher frequency vibration modes. A more general model was proposed by Elvin et al. [46,47] which was capable of accommodating multiple vibration modes but required accurate mode assumptions and significant computational expense. Another notable contribution was made by Yang et al. [48], who developed the ECM to connect structural and electrical simulation, providing a comprehensive representation of piezoelectric energy harvesters. Nevertheless, their model heavily relied on finite element analysis to set correct circuit parameters. Lumped parameter model (LPM) also treats the harvester as an SDOF system, following pioneering work of Williams et al. [49] in modeling the electromagnetic harvesters. However, due to inherent differences between electromagnetic and piezoelectric conversion mechanisms, the applicability of LPM to piezoelectric harvesters is limited [50–52]. Weinberg [53] developed this model tailored specifically to piezoelectric beams, providing a simplified representation of their behaviors. Nevertheless, their model neglects the electromechanical coupling and is limited to a single vibration mode. Accurately predicting the optimal coupled electromechanical output, as observed by Roundy et al. [54] and Dutoit et al. [55], remains a challenge. Erturk et al. [56] critically pointed out the inaccuracies and limitations of the LPM and analyzed the specific reasons. In subsequent work, Erturk [57] proposed a generalized framework for the electromechanical modeling of piezoelectric energy harvesters using the assumed-modes method.

In recent years, the finite element method (FEM) has been widely used as a vital tool for solving complex mathematical physics problems due to the availability of commercial finite element software. Compared to previous SDOF models, FEM provides a more accurate and convenient prediction of output performances of piezoelectric beams. Wang et al. [58] created a simulation model for both static and dynamic analysis of bimorph piezoelectric beams using FEM. By dividing the thickness of the beam into smaller sections, they were able to determine the actual nonlinear distribution and predict both overall and localized responses. Thein et al. [59] followed a similar approach and developed an FE model for bimorph piezoelectric beams. They adjusted key terms to meet FEM requirements and formulated an output power formula based on the load voltage formula derived by Roundy et al. [60]. Poya et al. [34] proposed a general hp-FEM framework for linear piezoelectric beams,

handling both static and dynamic scenarios. Givois et al. [61] proposed a reduced-order modeling method based on a three-dimensional FE formulation to predict the dynamics of piezoelectric structures with geometric nonlinearities, thereby simplifying the FEM. The use of FEM for geometric parameter design and structural optimization of piezoelectric energy harvesters has gained significant attention in recent years [62–64], driven by advancements in computational technology. Nevertheless, as a numerical method, FEM often cannot simultaneously achieve high efficiency and precision. Especially when simulating the coupled dynamic response of structures in the high-frequency range, there is a significant computational cost. Therefore, it is crucial to develop a more efficient analytical model for predicting the electromechanical response of piezoelectric beams.

To address the limitations mentioned above, it is necessary to establish a suitable and accurate model. Erturk et al. [65–67] proposed the distributed parameter model (DPM) for piezoelectric beams based on the analytical solution of coupled electromechanical system equations which can provide a more accurate representation of the behavior of piezoelectric beams. Abdelkef et al. [68] proposed a global nonlinear reduced-order model based on Galerkin discretization. However, the model could not accurately evaluate the performance of harvesters due to the neglect of piezoelectric properties and electric effects. Further research and refinement of the model are necessary to account for these factors and improve the predictive capabilities of DPM. Carrera et al. [69] developed the FEM with node-dependent kinematics (NDK) by applying Carrera unified formulation (CUF) to the static analysis of piezoelectric beams. Building on this, Zappino et al. [70] extended the application of NDK to the dynamic analysis of such structures. Based on the CUF, the 3D displacement field can be elegantly expanded using generalized unknown variables of any order across the cross-section. Moreover, the order of expansions can be treated as an independent parameter, which is determined by the specific problem being considered. Bonello and Neubert et al. [71] have advocated for the dynamic stiffness method (DSM), also known as the spectral finite element method (SFEM) [72], or spectral element method (SEM) [73–75] as a powerful tool for deriving the frequency response function (FRF) of structural elements with constant cross-sections and their combinations [76–79]. DSM involves the establishment of an element dynamic stiffness matrix based on the exact solutions of governing differential equations. The shape function of DSM is defined as the homogeneous solution of the governing differential equation in the frequency domain, in contrast to FEM where the basis function is typically composed of lower order polynomials. Lee et al. [73] developed a spectral finite element model for intelligent material structures and derived the dynamic stiffness matrix for bimorph piezoelectric beams which can provide precise solutions while mitigating computational burdens. Park et al. [75] employed SFEM based on the Euler–Bernoulli beam and Timoshenko beam theories to analyze the dynamic response of bimorph piezoelectric beams and simulate the electromechanical coupling behavior of piezoelectric wafers, validating the effectiveness of SFEM through numerical examples in both time and frequency domains.

Against the above context, this paper develops an exact and efficient analytical modeling approach to accurately predict the electromechanical coupling response of piezoelectric beams based on the research of Bonello et al. [40]. The proposed method is employed for modal analysis and vibration energy harvesting analysis of the multimodal piezoelectric beams. The innovations of this paper include the following key aspects: (i) The dynamic stiffness (DS) model for piezoelectric beams is developed based on exact solution of the governing differential equations, eliminating spatial discretization and significantly reducing DoFs to enhance computational efficiency. (ii) Compared to the research of other scholars [40,65,67,71,75], this paper proposes the DS model for the piezoelectric beams with three typical tip attachments and external circuits, enabling a more comprehensive multimodal analysis of the harvesting structures. (iii) The Wittrick–Williams (WW) algorithm enables accurate eigenvalue computation with arbitrary
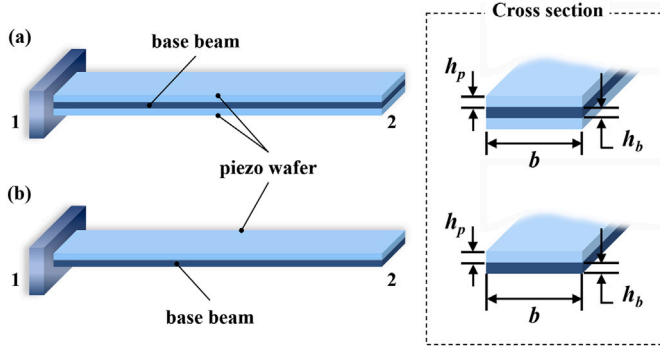
Fig. 1. Cantilever structure of piezoelectric beams with (a) bimorph and (b) unimorph.

precision, efficiently handling complex boundary conditions and high-order modes. This algorithm can be further employed to adjust the structural natural frequencies to match environmental vibration, thereby improving energy harvesting effect in a highly efficient and reliable manner. (iv) The electrically-induced stiffness and electrically-induced damping are introduced to facilitate the description of the impact of energy harvesting circuits on the piezoelectric structures. (v) The proposed method is applicable for analyzing the electromechanical coupling output effects of piezoelectric beams under different structural and material parameters. Furthermore, the DSM can be extended to more complex energy harvesting structures and combined with high-order beam models [80]. This enables accounting for the influence of thickness stretching of the piezoelectric structure on vibration energy harvesting and conducting a more comprehensive and accurate analysis of the electromechanical coupling response of piezoelectric beams.

This paper is structured into four sections, encompassing the introduction above. Section 2 outlines the derivation of the DS matrices for piezoelectric beams and introduces the Wittrick–Williams algorithm for solving eigenvalues of the DS matrices. Section 3 validates the proposed models and explores the effects of different structures and parameters on the energy harvesting efficiency of piezoelectric beams. Lastly, the main conclusions of this paper are summarized in Section 4.

2. Theory

The dynamic stiffness method for the electromechanical coupling modeling of piezoelectric beams will be introduced in Section 2.1. Then the response analysis of piezoelectric beams under base excitation using the dynamic stiffness method will be conducted in Section 2.2. Lastly, the Wittrick–Williams (WW) algorithm will be developed in Section 2.3 as a reliable method for resonant frequency computation.

2.1. Dynamic stiffness modeling of piezoelectric beams

The dynamic stiffness (DS) matrices of piezoelectric beams with different tip attachments and external circuits will be derived in this section. In addition, the segmented-electrode piezoelectric beam will be taken as an example to introduce the assembly procedure of DS matrices, expanding the application scope of the proposed method.

2.1.1. DS modeling of cantilevered piezoelectric beams with three different tip attachments

Firstly, the cantilevered piezoelectric beams without external circuits as schematically depicted in Fig. 1 will be considered and the DS matrices of piezoelectric beams with three different tip attachments will be derived.

The governing differential equation of piezoelectric beam can be rewritten as follows (see also Appendix A)

$$(YI)_{\text{eff}} \frac{\partial^4 w}{\partial x^4} + (\rho A)_{\text{eff}} \frac{\partial^2 w}{\partial t^2} = 0 \tag{1}$$

where $w(x, t)$ represents the displacement of piezoelectric beams at position x and time t. Y, I and ρ represent the Young's modulus, the cross-sectional moment of inertia, and density of the material, respectively. $(YI)_{\text{eff}}$ and $(\rho A)_{\text{eff}}$ respectively represent bending stiffness and mass per unit length of the bimorph and unimorph piezoelectric beams, as shown below

$$(YI)_{\text{eff}}^{\text{b}} = Y_{\text{b}} I_{\text{b}}^{\text{b}} + 2Y_{\text{p}} I_{\text{p}}^{\text{b}}, \quad (\rho A)_{\text{eff}}^{\text{b}} = b(\rho_{\text{b}} h_{\text{b}} + 2\rho_{\text{p}} h_{\text{p}}) \tag{2a}$$

$$(YI)_{\text{eff}}^{\text{u}} = Y_{\text{b}} I_{\text{b}}^{\text{u}} + Y_{\text{p}} I_{\text{p}}^{\text{u}}, \quad (\rho A)_{\text{eff}}^{\text{u}} = b(\rho_{\text{b}} h_{\text{b}} + \rho_{\text{p}} h_{\text{p}}) \tag{2b}$$

where the subscripts $(\cdot)_{\text{b}}$ and $(\cdot)_{\text{p}}$ respectively represent the base beam and piezoelectric wafer. The superscripts $(\cdot)^{\text{b}}$ and $(\cdot)^{\text{u}}$ represent the bimorph and unimorph piezoelectric beams, respectively. Four moments of inertia about the neutral axis are shown as follows

$$I_{\text{b}}^{\text{b}} = b h_{\text{b}}^3/12, \quad I_{\text{p}}^{\text{b}} = b \left[\left(h_{\text{p}} + h_{\text{b}}/2 \right)^3 - \left(h_{\text{b}}/2 \right)^3 \right]/3 \tag{3a}$$

$$I_{\text{b}}^{\text{u}} = b(p_{\text{b}}^3 - p_{\text{a}}^3)/3, \quad I_{\text{p}}^{\text{u}} = b(p_{\text{c}}^3 - p_{\text{b}}^3)/3 \tag{3b}$$

where p_{a}, p_{b} and p_{c} denote the locations of the bottom of the base beam, the bottom of the piezo wafer and the top of the piezo wafer from the neutral axis, respectively, as shown below

$$p_{\text{a}} = -\frac{h_{\text{p}}^2 + 2h_{\text{p}}h_{\text{b}} + nh_{\text{b}}^2}{2\left(h_{\text{p}} + nh_{\text{b}}\right)}, \quad p_{\text{b}} = \frac{h_{\text{p}}^2 + 2\,nh_{\text{p}}h_{\text{b}} + nh_{\text{b}}^2}{2\left(h_{\text{p}} + nh_{\text{b}}\right)} - h_{\text{p}},$$

$$p_{\text{c}} = \frac{h_{\text{p}}^2 + 2\,nh_{\text{p}}h_{\text{b}} + nh_{\text{b}}^2}{2\left(h_{\text{p}} + nh_{\text{b}}\right)} \tag{4}$$

Assuming a harmonic excitation with frequency ω, let $W(\xi)$ represent the complex amplitude of deflection w as follows

$$w(\xi, t) = W(\xi) e^{i\omega t} \tag{5}$$

where $\xi = x/L$. By substituting the time domain variable in Eq. (1) with the frequency domain variable in Eq. (5), the motion equation for piezoelectric beam can be represented as follows

$$\frac{d^4 W}{d\xi^4} - \lambda^4 W = 0, \quad \lambda = \sqrt[4]{\frac{\omega^2 L^4 (\rho A)_{\text{eff}}}{(YI)_{\text{eff}}}} \tag{6}$$

Referencing the DS matrix in Appendix A, while adding boundary conditions for forces and displacements, and eliminating the constant vectors, the DS matrix for the piezoelectric beam can be derived as follows

$$\mathbf{K} = \begin{bmatrix} d_1 & d_2 & d_4 & d_5 \\ d_2 & d_3 & -d_5 & d_6 \\ d_4 & -d_5 & d_1 + \triangle & -d_2 \\ d_5 & d_6 & -d_2 & d_3 \end{bmatrix} \tag{7}$$

where $d_1 \sim d_6$ are frequency relevant terms which are provided in Appendix A.

Additionally, this paper has formulated DS matrices for the unimorph/bimorph piezoelectric beams with three different tip attachments as illustrated in Table 1. Here, M_T and K_T represent lumped mass attached above the beam and stiffness coefficient of the spring, respectively.

In the case of a piezoelectric beam with a primary mass, the term $-\omega^2 M_T$ is added to the degree of freedom (DoF) associated with the transverse displacement of node 2. This adjustment takes into account

the presence of a tip mass and modifies the DS matrix accordingly. Similarly, for a piezoelectric beam equipped with a tip spring of stiffness K_T, the spring stiffness coefficient K_T is incorporated into the relevant DoF of node 2 to calculate the DS matrix. This incorporation ensures that the DS matrix accurately represents the impact of the tip mass and spring on the overall dynamic behavior of the piezoelectric beam.

Furthermore, in the context of a piezoelectric beam with a spring-mass oscillator subjected to harmonic vibration, the interconnection between nodes 1 and 2 signifies the beam, while the interconnection between nodes 2 and 3 symbolizes the spring. By combining the DS matrices of these two components, the DS matrix of the overall structure can be obtained and expressed as follows

$$\begin{bmatrix} F_{y2} \\ M_2 \\ F_{y3} \end{bmatrix} = \begin{bmatrix} d_1 + K_T & -d_2 & -K_T \\ -d_2 & d_3 & 0 \\ -K_T & 0 & K_T - \omega^2 M_T \end{bmatrix} \begin{bmatrix} W_{y2} \\ \theta_2 \\ W_{y3} \end{bmatrix} \tag{8}$$

Eq. (8) can also be expressed as a 2×2 matrix by converting the displacement at node 3 in spring-mass system to node 2 as shown below

$$\begin{bmatrix} F_{y2} \\ M_2 \end{bmatrix} = \begin{bmatrix} d_1 + \frac{-\omega^2 M_T K_T}{K_T - \omega^2 M_T} & -d_2 \\ -d_2 & d_3 \end{bmatrix} \begin{bmatrix} W_{y2} \\ \theta_2 \end{bmatrix} \tag{9}$$

In summary, for piezoelectric beams with various tip attachments, the DS matrices only need to incorporate $\triangle$ in Eq. (7) into the corresponding DoF linked to the transverse displacement of node 2.

2.1.2. DS modeling of different vibration energy harvesting circuits

The DS modeling of piezoelectric beams with three representative external circuits as schematically depicted in Fig. 2 will be developed. It is assumed that the electrodes affixed uniformly to the beam are thin, flexible, highly conductive, and possess minimal resistance.

Piezoelectric vibration energy harvesting is achieved through utilization of positive piezoelectric effect exhibited by piezoelectric materials which is commonly described using four types of constitutive

Table 1
The piezoelectric beams with different tip attachments.

Tip attachments	Primary mass	Spring	Spring-mass oscillator
$\triangle$	$-\omega^2 M_T$	K_T	$\frac{-\omega^2 M_T K_T}{K_T - \omega^2 M_T}$
Bimorph			
Unimorph			

equations [81]. In this paper, the modeling of energy harvesting beams is based on the type d piezoelectric constitutive equation, represented as follows

$$\delta = \sigma_p/Y_p + d_{31} E_3 \tag{10a}$$

$$D_3 = d_{31} \sigma_p + \varepsilon_{33}^\sigma E_3 \tag{10b}$$

where Y_p, d_{31}, and ε_{33}^σ represent the Young's modulus, piezoelectric coefficient, and permittivity at constant stress of the piezoelectric material, respectively. D_3 denotes the electric displacement, and E_3 represents the electric field induced by deformation. The strain δ of the piezoelectric layer at a given distance z from the neutral axis can be expressed as

$$\delta = -z \frac{\partial^2 w}{\partial x^2} \tag{11}$$

The stress of the piezoelectric wafer and base beam can be expressed as follows

$$\sigma_p = Y_p \delta - d_{31} Y_p E_3, \quad \sigma_b = Y_b \delta \tag{12}$$

Then, the total stress σ can be expressed as the combination of σ_p and σ_b as follows

$$\sigma = \sigma_p + \sigma_b = -z(Y_p + Y_b) \frac{\partial^2 w}{\partial x^2} - d_{31} Y_p E_3 \tag{13}$$

where E_3 is the electric field which can be expressed by the generated voltage $V(t)$

$$E_3 = -\frac{V(t)}{a h_p} \tag{14}$$

The value of a is either 1 or 2 depending on the external circuits of the piezoelectric beam as shown in Table 2.

Substituting the stress σ_p into Eq. (10b), and considering the strain δ at the middle section of the piezo layer for $h_{pm} = (h_b + h_p)/2$, the electric displacement $D_3(x,t)$ can be obtained as follows

$$D_3(x,t) = -d_{31} Y_p h_{pm} \frac{\partial^2 w}{\partial x^2} - \varepsilon_{33}^S \frac{V(t)}{a h_p} \tag{15}$$

where $\varepsilon_{33}^S = \varepsilon_{33}^\sigma - d_{31}^2 Y_p$. The charge generated by the polarization of the piezoelectric material can be determined by integrating the electric
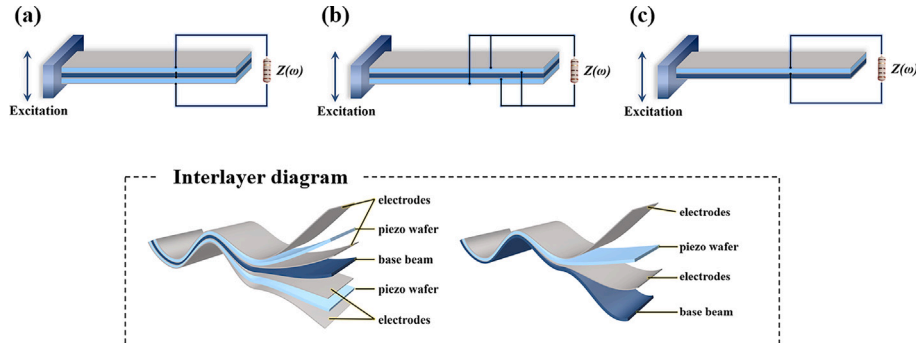
Table 2
The piezoelectric beams with different circuits.

Different models	a	f	ϑ
Series bimorph	2	1	$-d_{31} Y_p b (h_p + h_b)/a$
Parallel bimorph	1	2	$-d_{31} Y_p b (h_p + h_b)/a$
Unimorph	1	1	$-d_{31} Y_p b (p_c^2 - p_b^2)/2h_p$

Fig. 2. Base-excited piezoelectric energy harvesting beams with external circuits: (a) series-connected bimorph, (b) parallel-connected bimorph, and (c) unimorph.

displacement **D** with the outward unit normal **n**.

$$q(t) = \int_A \mathbf{D} \cdot \mathbf{n} dA = -\int_{x=0}^L \left(d_{31} Y_p h_{pm} b \frac{\partial^2 w}{\partial x^2} + \varepsilon_{33}^S b \frac{V(t)}{ah_p} \right) dx \qquad (16)$$

The expression for the current i in the external circuit can be derived by differentiating the generated charge $q(t)$ with respect to time t

$$i(t) = \frac{dq(t)}{dt} = f\left(-d_{31} Y_p h_{pm} b \int_0^L \frac{\partial^3 w}{\partial x^2 \partial t} dx - \frac{\varepsilon_{33}^S bL}{ah_p} \dot{V} \right) \qquad (17)$$

where f is either 1 or 2, depending on the external circuits of the piezoelectric beam as specified in Table 2. The output voltage of the piezoelectric cantilever beam can be calculated by multiplying the load impedance Z with the current $i(t)$ as follows

$$V = i(t)Z = G \int_0^L w'' dx = G(\theta_L - \theta_0) \qquad (18)$$

where G is a complex number. It should be emphasized that G can be separated into the imaginary part G_i and the real part G_r as depicted below

$$G = \frac{i\omega f \beta}{i\omega(f/a)C_p + 1/Z} = G_r + iG_i \qquad (19a)$$

$$\beta = -d_{31} Y_p h_{pm} b, \quad C_p = \varepsilon_{33}^S bL/h_p \qquad (19b)$$

where G_i and G_r respectively introduce the electrically-induced damping and the electrically-induced stiffness to the piezoelectric energy harvesting beam, which will be explained in detail later.

The bending moment M of the piezoelectric beam can be calculated by integrating the cross-sectional area A with the product of stress σ and $-z$ shown as follows

$$M(x,t) = \int -\sigma z dA = (YI)_{\text{eff}}^{\text{b}} \frac{\partial^2 w}{\partial x^2} + \vartheta V(t) \qquad (20)$$

where ϑ is depending on the type of energy harvesting circuits, as shown in Table 2. Thus, the DS matrix of the piezoelectric beam with energy harvesting circuits can be developed as

$$\mathbf{K} = \begin{bmatrix} d_1 & d_2 & d_4 & d_5 \\ d_2 & d_3 & -d_5 & d_6 \\ d_4 & -d_5 & d_1 + \triangle & -d_2 \\ d_5 & d_6 & -d_2 & d_3 \end{bmatrix} + \vartheta G \begin{bmatrix} 0 & 0 & 0 & 0 \\ 0 & 1 & 0 & -1 \\ 0 & 0 & 0 & 0 \\ 0 & -1 & 0 & 1 \end{bmatrix} \qquad (21)$$

where the first matrix represents the physical stiffness matrix of the piezoelectric structure without considering piezoelectric effect, whereas the second matrix related to ϑG denoted by Eq. (19a) introduces the electrically-induced stiffness ϑG_r and electrically-induced damping ϑG_i to the piezoelectric structure as shown below

$$\vartheta G = \vartheta G_r + i\vartheta G_i \qquad (22a)$$

$$\vartheta G_i = \frac{\vartheta \omega f \beta}{1/Z + \omega^2 (f/a)^2 C_p^2 \, Z}, \qquad \vartheta G_r = \frac{\vartheta \omega^2 f (f/a) \beta C_p}{1/Z^2 + \omega^2 (f/a)^2 C_p^2} \qquad (22b)$$

The expressions of ϑG_i and ϑG_r clearly demonstrate that the load resistance Z has an impact on the electrically-induced stiffness and damping. As the load resistance increases, the stiffness demonstrates an upward trend, while the damping initially increases and then decreases. In other words, there exists a resistance value Z_m that optimizes the electrically-induced damping. The formula for this resistance value is as follows:

$$Z_m = \sqrt{\frac{1}{\omega^2 (f/a)^2 C_p^2}} \qquad (23)$$

To provide clarity, we introduce the concepts of physical stiffness $(YI)_{\text{eff}}$, electrically-induced stiffness ϑG_r, and electrically-induced stiffness ϑG_i. The physical stiffness is determined by the elastic modulus and
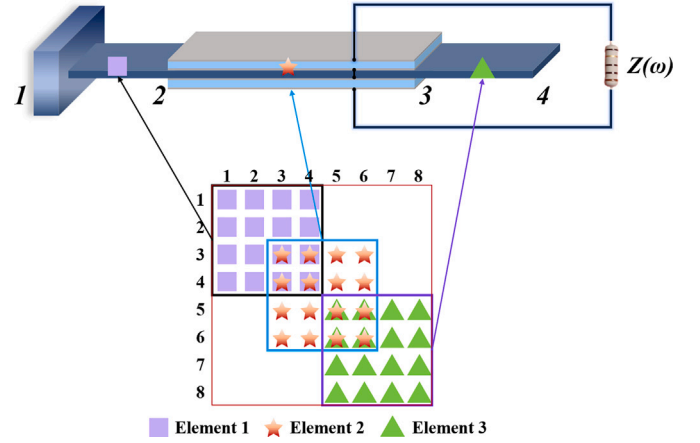

Fig. 3. Assembly diagram of dynamic stiffness matrices for segmented-electrode piezoelectric beams.

dimensions of the piezoelectric wafers and base beam. The electrically-induced stiffness refers to the impact on the overall cantilever structure when a piezoelectric cantilever beam is connected to an external circuit, as compared to its stiffness without circuit. Electrically-induced damping is generated by converting mechanical energy into electrical energy through the piezoelectric energy harvester. Optimizing this equivalent damping enhances the energy harvesting efficiency. These concepts explain how the presence of piezoelectric wafers and external circuits affect the energy conversion efficiency of piezoelectric beams.

2.1.3. DS modeling of segmented-electrode piezoelectric beam

The dynamic stiffness method has significant advantages in the modeling of built-up beam structures and in conducting free vibration and modal response analysis. The DS formulation for the segmented-electrode piezoelectric cantilever beam will be developed as an example to introduce the modeling and assembly process of DS matrices.

As shown in Fig. 3, when the range of PZT covering the elastic beam is from $x = x_1$ to $x = x_2$ instead of covering the entire length of beam, the DS matrix of each element can be obtained by dividing the beam elements, and then the DS matrices can be assembled to form the global DS matrix for the segmented-electrode piezoelectric beam. This assembly procedure allows each beam element to have different cross-sections and lengths, making it suitable for modeling segmented-electrode piezoelectric beams with any boundary conditions.

Firstly, the entire structure is divided into three sub-structures at the boundary of two cross-sections of the segmented-electrode piezoelectric beam. Next, the DS matrices of each beam element are derived. Element 2 located between nodes 2 and 3 represents a piezoelectric beam, and its element DS matrix is shown in Eq. (21). Element 1 and 3 are single beams, and their DS matrix is shown in Eq. (7). Finally, the DS matrices of Element 1, 2 and 3 are assembled at the corresponding degrees of freedom to form an 8×8 global DS matrix. Due to the assembly process of the element DS matrices being similar to that of the FEM, the DSM can be extended to the modeling of other more complex built-up beam structures.

2.2. Response analysis of piezoelectric beam using dynamic stiffness method

The output voltage and tip displacement frequency response of piezoelectric energy harvesting beam under a given base excitation can be analyzed by using both the dynamic stiffness method (DSM), as described in this section compared to the dynamic flexibility method (DFM) [40], also described in Appendix B.

The DS matrix of the piezoelectric beam, as depicted in Eq. (21), can be formulated as follows

$$
\begin{bmatrix} F_0 \\ M_0 \\ F_L \\ M_L \end{bmatrix} = \begin{bmatrix} k_{11} & k_{12} & k_{13} & k_{14} \\ k_{21} & k_{22} & k_{23} & k_{24} \\ k_{31} & k_{32} & k_{33} & k_{34} \\ k_{41} & k_{42} & k_{43} & k_{44} \end{bmatrix} \begin{bmatrix} W_0 \\ \theta_0 \\ W_L \\ \theta_L \end{bmatrix}
\tag{24}
$$

where k_{ij} represents the element in the row i and column j of DS matrix **K**. For the piezoelectric beam with base-excitation, there is no input excitation at the other tip, so set the F_L and M_L in the above formula to zero and we can obtain

$$
\begin{bmatrix} W_L \\ \theta_L \end{bmatrix} = -\frac{1}{k_{33}k_{44} - k_{43}k_{34}} \begin{bmatrix} k_{44}k_{31} - k_{34}k_{41} & k_{44}k_{32} - k_{34}k_{42} \\ -k_{43}k_{31} + k_{33}k_{41} & -k_{43}k_{32} + k_{33}k_{42} \end{bmatrix}
$$
$$
\times \begin{bmatrix} W_0 \\ \theta_0 \end{bmatrix}
\tag{25}
$$

Thus, the output voltage and displacement of the piezoelectric cantilever beam with a tip primary mass can be represented by base excitation W_0 and θ_0 as follows

$$
V = G\left[(k_{43}k_{31} - k_{33}k_{41})/\alpha\right]W_0 + G\left[(k_{43}k_{32} - k_{33}k_{42} - \alpha)/\alpha\right]\theta_0 \tag{26a}
$$

$$
W_L = \left[-(k_{44}k_{31} - k_{34}k_{41})/\alpha\right]W_0 + \left[-(k_{44}k_{32} - k_{34}k_{42})/\alpha\right]\theta_0 \tag{26b}
$$

where $\alpha = k_{33}k_{44} - k_{43}k_{34}$.

In comparison to the DFM [40], also outlined in Appendix B for analyzing the responses of piezoelectric cantilevered beam, the proposed DSM presents significant advantages as it is stiffness based where the aforementioned electrically-induced stiffness and damping are in the form of dynamic stiffness with very clear physical meanings and the elements can be directly assembled to model generally complex beam built-up structures. Moreover, the DS matrix can be directly employed for eigenvalue computation by using the Wittrick–Williams algorithm, thereby obtaining the natural frequencies of the piezoelectric beam. In addition, unlike the DFM [40], which may encounter numerical singularity issues in matrix inversion during the eigenvalue and response-solving processes, the DSM is proven to be robust against such numerical challenges. Consequently, the DSM emerges as a more reliable and efficient approach for tackling complex beam built-up structural analyses.

2.3. Wittrick–Williams algorithm for resonant frequency computation

Piezoelectric energy harvesters can achieve maximum output voltage when operating at their resonant frequency. Therefore, it is common practice to tune the natural frequency of the piezoelectric beam in the design of these energy harvesters to match the ambient vibration frequency. By deriving the DS matrices for piezoelectric beams with different tip attachments, both unimorph and bimorph, the eigenvalues of these matrices can be calculated using the Wittrick–Williams (WW) algorithm [82]. This algorithm, known for its accurate and efficient computation of eigenvalues for DS matrices, provides a powerful tool for frequency tuning of piezoelectric energy harvesting beams.

The WW algorithm is commonly used for computing eigenvalues of Hermitian matrices, which refer to matrices where the elements on the main diagonal are real numbers and the matrix is self-conjugate. The DS matrix of the piezoelectric beam as represented in Eq. (21) is actually not a Hermitian matrix, as its main diagonals contain the electrically-induced damping ϑG_i. Nevertheless, the impact of the imaginary part of ϑG on the DS matrix can be ignored since it is negligible compared to the stiffness terms d_3 and ϑG_r, which approach zero. It should be noted that although the DS matrix ignores the electrically-induced damping, it still includes the electrically-induced stiffness. It will be demonstrated in Sections 3.1 and 3.2 that the absolute values of electrically-induced

damping ϑG_i is much smaller than the electrically-induced stiffness ϑG_r and the dynamic stiffness of the piezoelectric beams without considering piezoelectric effect. The superposition of the later two stiffnesses is essentially symmetric matrix, which is clear from Eqs. (21) and (22), whereas the imaginary term $i\vartheta G_i$ is too small for the modal analysis and can be neglected, which is expected. Therefore, the WW algorithm can be extended to solve eigenvalues of the DS matrix of piezoelectric beam, even though the diagonal terms of the DS matrix has complex values.

The fundamental principle of the WW algorithm is to determine the number of natural frequencies of structures below a given test frequency $\omega^{\#}$. Its general formula can be expressed as follows

$$
J\left(\omega^{\#}\right) = J_0\left(\omega^{\#}\right) + s\left\{\mathbf{K}\left(\omega^{\#}\right)\right\} \tag{27}
$$

Firstly, select a test frequency, represented as $\omega^{\#}$. Calculate the corresponding DS matrix and apply the Gauss elimination method to convert the matrix into an upper triangular form. Next, count the number of elements smaller than zero on the main diagonal of the matrix and record it as the number of sign changes, denoted as $s\left\{\mathbf{K}\left(\omega^{\#}\right)\right\}$. This count indicates the number of structural natural frequencies that are lower than the test frequency. $J_0\left(\omega^{\#}\right)$ represents the number of natural frequencies or critical load factors that are lower than the test value when the structure is rigid, and it can be determined as follows

$$
J_0\left(\omega^{\#}\right) = \sum_{i=1}^{m} J_i\left(\omega^{\#}\right) \tag{28}
$$

After calculating $J\left(\omega^{\#}\right)$, the bisection method can be employed to iteratively approximate the natural frequency of the structure with any desired level of accuracy. The WW algorithm is a precise and effective method for solving eigenvalues. It employs a bisection method to systematically scan through frequencies, ensuring that no natural frequencies are missed during the solution process.

3. Results and discussions

The results of free vibration and frequency response of both the classical and segmented-electrode piezoelectric beams, calculated using the dynamic stiffness method (DSM) and the finite element method (FEM), will be presented in Section 3.1. Subsequently, the output voltage frequency response functions (FRFs) of the piezoelectric beams with three typical tip attachments will be obtained in Section 3.2, and the influence of different factors on energy harvesting efficiency will be examined in Section 3.3. All results will be obtained using the same computer equipped with an 11th Gen Intel(R) Core(TM) i7-11800 H @2.30 GHz and 16GB of memory.

3.1. Comparative analysis of DSM and COMSOL results

The results of the modal vibration and frequency response of the classical bimorph piezoelectric cantilever beam and the segmented-electrode piezoelectric beam, calculated using the DSM and FEM respectively, will be presented in this section. The DSM results will be validated with FEM by using the commercial software COMSOL Multiphysics. Additionally, the influence of the electrically-induced stiffness and damping on the piezoelectric beam will also be analyzed in this section.

3.1.1. Modal and response analysis of the classical piezoelectric cantilever beams

The key dimensional and material parameters of the classical bimorph piezoelectric beam can be found in Table 3. Table 4 displays the first ten natural frequencies of piezoelectric beams, obtained using the DSM and FEM. Table 4 also presents the relative errors between the two sets of results which show that the two methods produce consistent results. The slight disparities between the DSM and COMSOL

Table 3
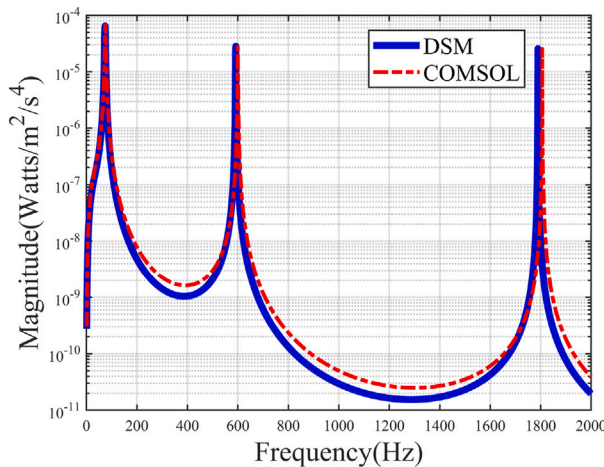Dimensional and material parameters of the piezoelectric beam.

Components	Piezo layer	Base beam	Variables	Unit
Material	PZT-5 H	Aluminium	–	–
Density	7800	2700	ρ_p/ρ_b	kg/m³
Length	60	60	L	mm
Thickness	0.267	0.3	h_p/h_b	mm
Width	5	5	b	mm
Elastic modulus	62	72	Y_p/Y_b	GPa
Piezoelectric coefficient	−320	–	d_{31}	pm/V
Piezoelectric permittivity	3.363×10^{-8}	–	ε_{33}^T	nF/m

can be attributed to the differences in the modeling approaches. In this paper, the DS modeling of the piezoelectric beams is based on the Euler–Bernoulli beam model, while in COMSOL, beam modeling relies on solid mechanics physical fields.
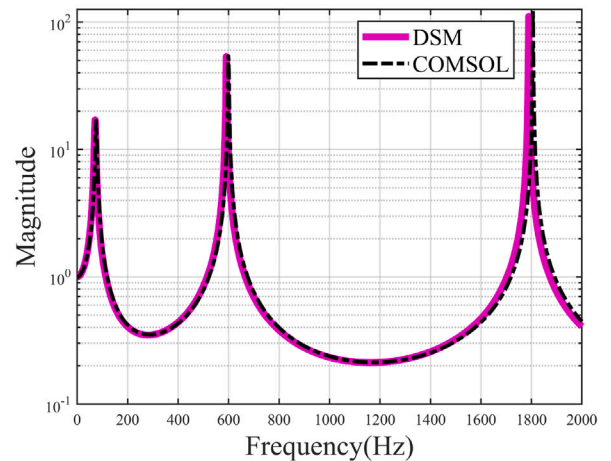
Our attention then shifts to the parallel-connected bimorph piezoelectric cantilever beams with a tip mass, referred to as $M_T = 0.5m_b$, and a pure resistance impedance of $Z = 100\ k\Omega$. Fig. 4(a) shows the power frequency response functions (FRFs) of the piezoelectric beam generated per unit amplitude base acceleration by the DSM and COMSOL. Furthermore, Fig. 4(b) presents the tip displacement of the piezoelectric beam, also generated per unit amplitude base acceleration by the DSM and COMSOL. This displacement FRF represents the transmissibility connecting W_L and W_0.

The graphs clearly show that the piezoelectric beam's peak output powers consistently occur at its natural frequencies, with a decline in amplitude as the frequency increases. It is worth noting that the DSM curve closely matches the FEM results near the natural frequencies. However, between the two peaks, the output power FRF of FEM is slightly higher than that of DSM. The output power and tip displacement amplitudes of the piezoelectric beam at its three resonance peaks are presented in Table 5. It can be seen from the table that the amplitude results obtained by the DSM and the FEM are in excellent agreement, with a relative error of less than 5 %. In summary, compared to the FEM, the DSM reduces the calculated DoFs by 5 orders of magnitude, with a computation time only 0.5 % of that required for FEM which highlights the significant advantages of the DSM in terms of both computational efficiency and accuracy.

3.1.2. The impact of electrically-induced stiffness and electrically-induced damping

The WW algorithm is used to calculate the eigenvalues of DS matrices, which allows for the determination of natural frequencies for six representative beam types. The natural frequencies of these beam types are listed in Table 6 and depicted in Fig. 5, including a single beam, unimorph and bimorph piezoelectric beams without an external circuit, unimorph piezoelectric beams with an external circuit, and series- and parallel-connected piezoelectric beams.

Additionally, we use the DSM to draw the output power FRF curve of the piezoelectric beams with three typical external circuits as shown

Table 4
The influence of external circuit types on the natural frequency of piezoelectric beams (Hz).

Circuit type	Series bimorph			Parallel bimorph			Unimorph		
Method	DSM	FEM		DSM	FEM		DSM	FEM	
Mode order	f (Hz)	f (Hz)	R.E. (%)	f (Hz)	f (Hz)	R.E. (%)	f (Hz)	f (Hz)	R.E. (%)
ω_1	71.007	71.819	−1.13 %	73.582	75.156	−2.09 %	54.389	54.478	−0.16 %
ω_2	591.32	593.09	−0.3 %	591.58	599.55	−1.33 %	448.33	452.5	−0.92 %
ω_3	1789.1	1800.4	−0.63 %	1789.2	1806.2	−0.94 %	1358	1375	−1.24 %
ω_4	3661.0	3682.3	−0.58 %	3661.0	3687.9	−0.73 %	2780.7	2814.4	−1.2 %
ω_5	6211.8	6237.9	−0.42 %	6211.8	6243.6	−0.51 %	4718.9	4771.8	−1.11 %
ω_6	9441.9	9456.3	−0.15 %	9441.9	9466.1	−0.26 %	7173.2	7242.6	−0.96 %
ω_7	13,352	13,342	0.075 %	13,352	13,346	0.045 %	10,144	10,194	−0.49 %
ω_8	17,941	17,868	0.41 %	17,941	17,873	0.38 %	13,631	13,745	−0.83 %
ω_9	23,210	23,029	0.79 %	23,210	23,033	0.77 %	17,635	17,732	−0.55 %
ω_{10}	29,159	28,809	1.2 %	29,159	28,814	1.19 %	22,155	22,216	−0.27 %
DoFs	4	449,384	–	4	456,235	–	4	288,302	–
Computing time	0.54 s	116 s	–	0.53 s	119 s	–	0.47 s	91 s	–

(a) Output power

(b) Tip displacement

Fig. 4. Output characteristic FRFs of parallel-connected bimorph piezoelectric beam by the proposed DSM and COMSOL.

Table 5

The response amplitudes of the parallel-connected bimorph piezoelectric beam at the first three frequencies.

FRF model	Output power			Tip displacement		
Method	DSM	FEM		DSM	FEM	
Mode order	f (Hz)	f (Hz)	R.E. (%)	f (Hz)	f (Hz)	R.E. (%)
1	5.43e−5	5.63e−5	3.6	15.9	15.4	3.2
2	1.85e−5	1.87e−5	1.1	46.9	48.5	3.3
3	1.09e−5	1.08e−5	0.9	88.5	91.6	3.4

in Fig. 6. By combining Figs. 5, 6 and Table 6, the following conclusions can be drawn: (i) Increasing the number of piezoelectric wafers on the base beam, from a single beam to a unimorph piezoelectric beam, and then to a bimorph piezoelectric beam, enhances the physical stiffness of the cantilevered structure. Consequently, the natural frequencies of the structure are elevated. (ii) The natural frequencies of unimorph and bimorph piezoelectric beams with circuits are higher than those without circuits. This is due to the inclusion of electrically-induced stiffness in the overall structural stiffness. (iii) Different types of external circuits affect the natural frequencies of piezoelectric beams. Specifically, the natural frequency of series-connected bimorph is slightly lower than that of parallel-connected bimorph piezoelectric beams. This difference arises from the higher electrically-induced stiffness of parallel bimorph compared to series bimorph. (iv) The parallel bimorph piezoelectric beam exhibits higher electrically-induced damping compared to the series bimorph, resulting in a decrease in the output power. This phenomenon can be observed in Fig. 6. (v) The electrically-induced stiffness has a greater impact on low-order natural frequencies compared to high-order natural frequencies. Generally, the influence of physical stiffness on structural stiffness is relatively larger than the effect of electrically-induced stiffness.

3.1.3. Modal and response analysis of the segmented-electrode piezoelectric beam

The total length of the segmented-electrode piezoelectric beam is 110 mm. The upper and lower piezoelectric wafers are symmetrically laid, and their length is 60 mm. The distance from the left side of the piezoelectric wafer to the fixed end of the beam is 20 mm, and the distance from the right side to the free end of the beam is 30 mm. In addition, the material parameters and thickness of the piezoelectric beam are consistent with those of the classical bimorph piezoelectric cantilever beam in Section 3.1.1. The specific parameter values are shown in Table 1. Table 7 shows the first ten modal shapes of the segmented-electrode piezoelectric beam plotted by the DSM and the FEM. It can be seen from the table that the modal shapes obtained by the DSM agree very well with those obtained by the FEM, and the error of the natural frequencies calculated by the two methods is within 2 %.
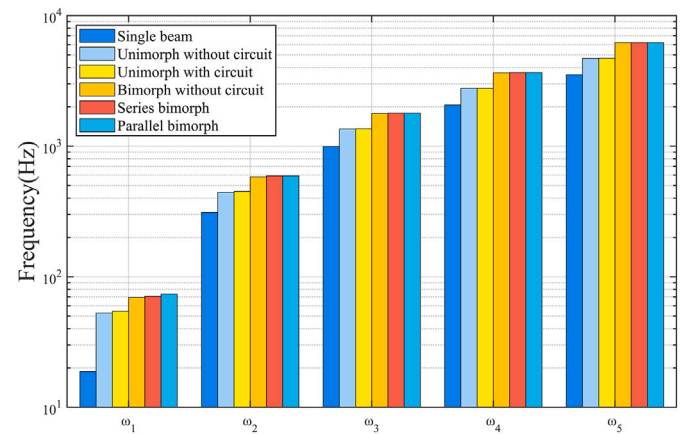

Fig. 5. Column schematic diagram of the first five natural frequencies of six different beam types.

The output power FRFs of the segmented-electrode piezoelectric beam are calculated by the DSM and FEM with a locally zoomed-in view near the first-order natural frequency, as shown in Fig. 7. It can be seen from the figure that the overall trends of the FRFs obtained by the two methods are consistent. However, there are some differences in the amplitudes at the natural frequencies. This is because the FEM is a numerical method and the factors such as mesh generation during the discretization process can lead to differences. Notably, an anti-resonance peak appears in the FRF between the second-order and third-order natural frequencies. This is due to the stiffness and mass distribution characteristics of the segmented-electrode piezoelectric beam and the electromechanical coupling effect of the piezoelectric material. These factors suppress the vibration energy of the system in this frequency range, resulting in the formation of the anti-resonance peak. In terms of calculation time, the DSM is two orders of magnitude faster than the FEM. This fully demonstrates that the proposed DSM has significant advantages in analyzing such piezoelectric built-up beams. The proposed method can be further used to establish an optimization model for the segmented-electrode piezoelectric beam to fully leverage its advantages.

3.2. Theoretical analysis of the piezoelectric beams with different tip attachments

DS models of series-connected piezoelectric beams with different tip attachments will be established in this section. Additionally, the influence of different structures on the power frequency response function of piezoelectric beams will be analyzed.

Initially, the piezoelectric beam is carrying a moderately sized primary mass $M_T = 0.5m_b$ at the tip with a pure resistance impedance
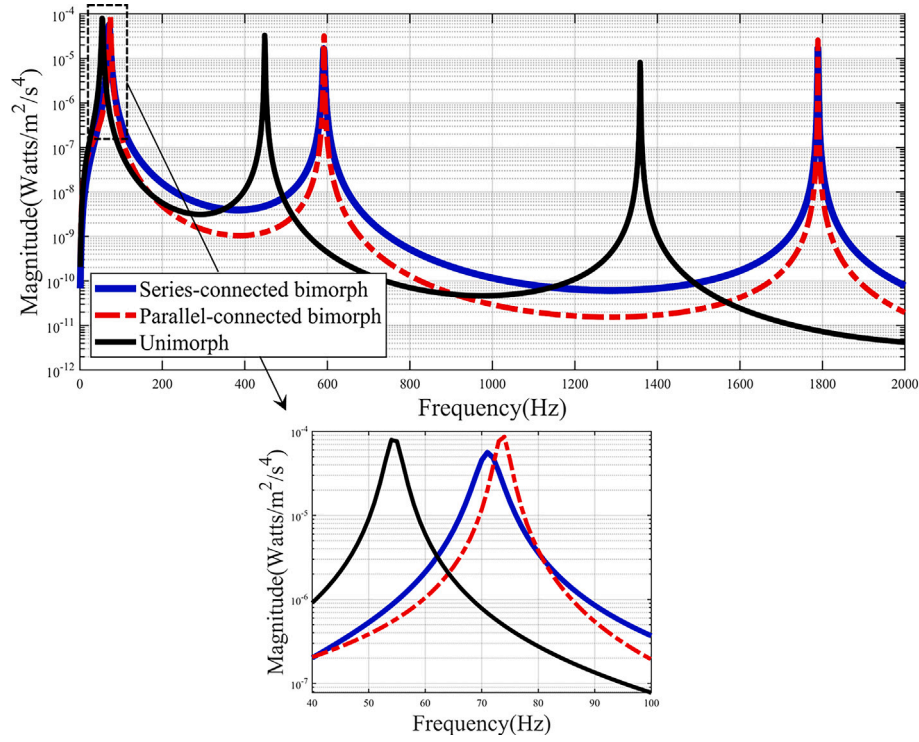
Table 6

The natural frequencies of different types of beams.

Beam types	Single beam	Unimorph	Unimorph with circuit		Bimorph	Series bimorph		Parallel bimorph	
B	$Y_b I_b$		$Y_b I_b + Y_p I_p$			$Y_b I_b + 2Y_p I_p$			
ϑG_r	–	–	$\frac{13.72\omega^2}{10^8 + 942\omega^2}$		–	$\frac{12.11\omega^2}{10^8 + 236\omega^2}$		$\frac{194.1\omega^2}{10^8 + 3768\omega^2}$	
ϑG_i	–	–	$\frac{4.47\omega}{10^5 + 0.942\omega^2}$		–	$\frac{7.91\omega}{10^5 + 0.236\omega^2}$		$\frac{31.64\omega}{10^5 + 3.768\omega^2}$	
Mode order	f (Hz)	f (Hz)	f (Hz)	R.E. (%)	f (Hz)	f (Hz)	R.E. (%)	f (Hz)	R.E. (%)
ω_1	18.83	52.766	54.389	3.08 %	69.446	71.007	2.25 %	73.582	5.96 %
ω_2	310.67	442.31	448.33	1.36 %	582.12	591.32	1.58 %	591.58	1.63 %
ω_3	994.16	1353.0	1358.4	0.39 %	1780.7	1789.1	0.47 %	1789.2	0.48 %
ω_4	2067.4	2775.5	2780.7	0.19 %	3652.9	3661	0.22 %	3661	0.22 %
ω_5	3530.9	4713.8	4718.9	0.11 %	6203.8	6211.8	0.13 %	6211.8	0.13 %
ω_6	5384.7	7168.2	7173.2	0.07 %	9434.1	9441.9	0.08 %	9441.9	0.08 %
ω_{10}	16,703	22,150	22,155	0.02 %	29,152	29,159	0.02 %	29,159	0.02 %

Fig. 6. Output power FRFs of the piezoelectric beam with different external circuits.

Table 7
The first 10 mode shapes of the segmented-electrode piezoelectric beam.

Method	1st	2nd	3rd	4th	5th
DSM	16.2783	204.894	359.574	869.379	1620.62
FEM	16.274	207.26	358.88	882.25	1626.9
	6th	7th	8th	9th	10th
DSM	2250.16	3526.01	4415.31	5206.34	6856.87
FEM	2261.1	3550.3	4422.3	5209.4	6893.5

$Z = 100 \ k\Omega$. By varying the magnitude of tip mass of the piezoelectric beam, the output power FRF near the first-order natural frequency of the beam can be obtained, as shown in Fig. 8(a). From the graph, it is evident that the first natural frequency decreases as the tip mass increases. Moreover, the peak amplitude of the output power corresponding to the first natural frequency increases with the mass.

Next, we consider the case where a spring is attached to the tip of the piezoelectric beam. As depicted in Fig. 8(b), it is evident that increasing the spring stiffness coefficient causes the first natural frequency of the piezoelectric beam to rise, while the peak output power remains relatively unchanged. In comparison to the scenario where the piezoelectric beam carries a tip mass, the output power frequency response function (FRF) of the beam with a spring at the tip exhibits a decrease in first-order anti-resonance before reaching the first resonance peak. Furthermore, as the spring stiffness coefficient increases, the anti-resonance peak gradually shifts towards the direction of the first resonance peak, resulting in a decrease in the gap between the peak and the valley.

The final case involves a piezoelectric cantilever beam with a spring-mass oscillator at the tip. By independently varying the mass M_T and the stiffness coefficient K_T of the oscillator, the output power FRF can be obtained as shown in Fig. 9. From the graphs, it can be seen that compared to the first two cases, this structure exhibits an additional first-order natural frequency, which corresponds to the natural frequency of the spring-mass oscillator. When the tip mass is changed individually, the first resonance peak changes similarly to the situation shown in Fig. 8(a), while the position of the second resonance peak and its corresponding output power remain basically unchanged. When the stiffness coefficient of the spring is changed separately, the first two natural frequencies show an upward trend. The first output power peak shows a decreasing trend, while the second output power peak remains basically unchanged as the stiffness coefficient increases.

3.3. Factors affecting the energy harvesting efficiency

The energy harvesting efficiency of piezoelectric beams can be influenced by both internal and external factors. In this section, we will
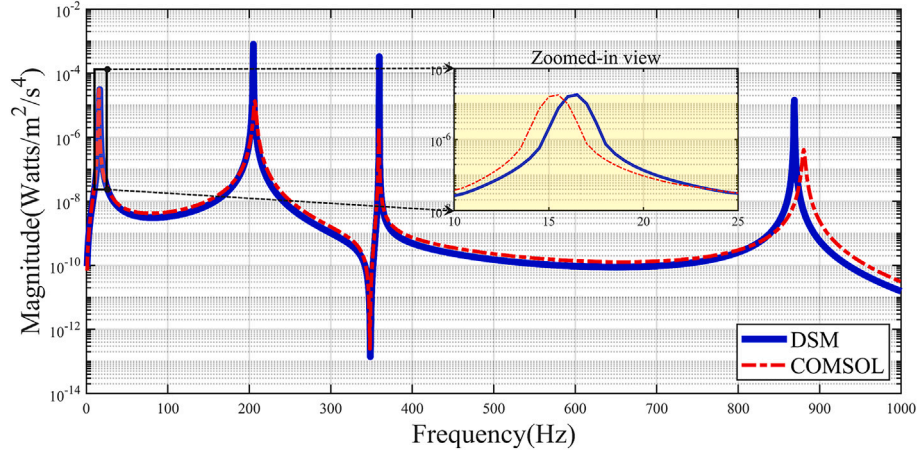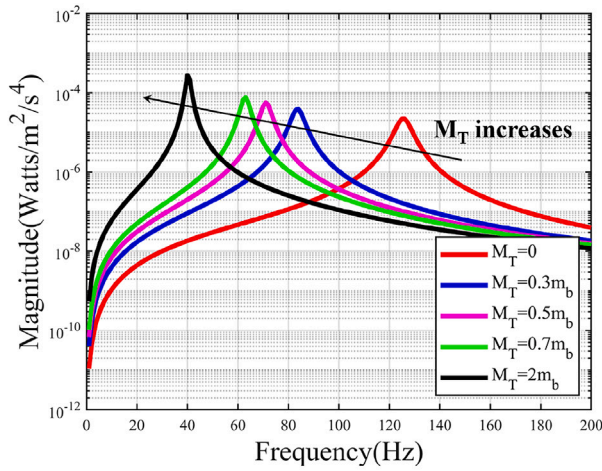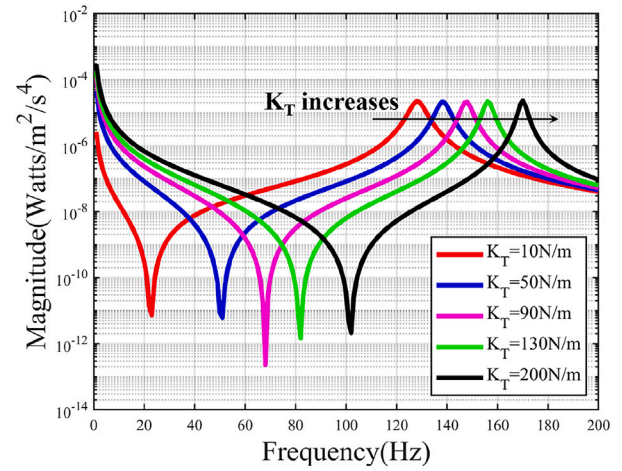
Fig. 7. Output power FRF of the segmented-electrode piezoelectric beam.

(a) With a tip mass

(b) With a spring

Fig. 8. Output power FRF of the piezoelectric beam.
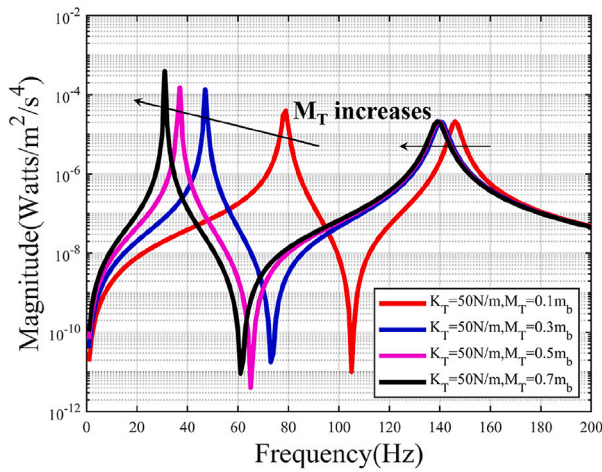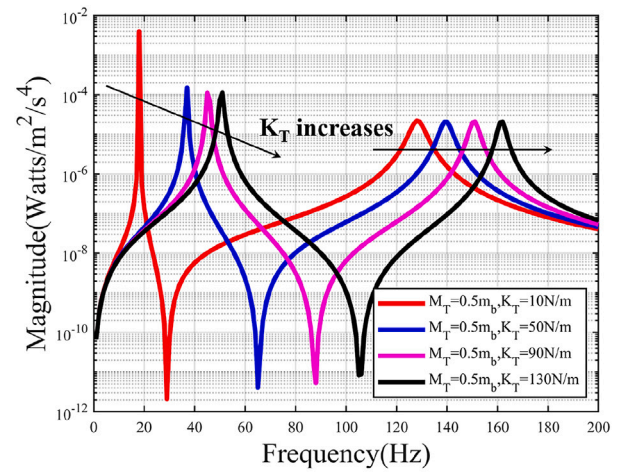

(a) Only change M_T

(b) Only change K_T

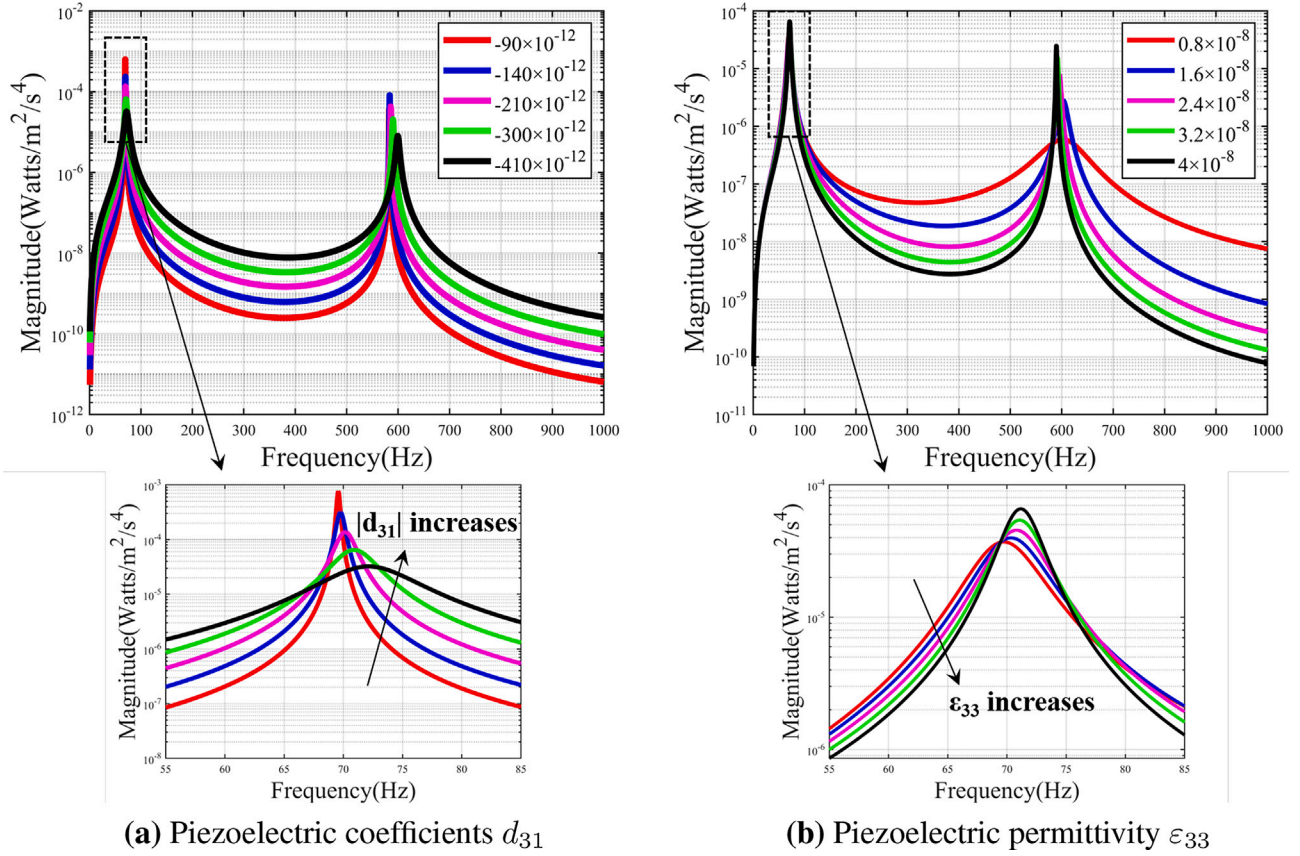**Fig. 9.** Output power FRF of the piezoelectric beam carrying a spring-mass system.

Fig. 10. Output power FRF of piezoelectric beams with different material parameters.

examine how various factors impact the energy harvesting of beams. The study focuses on the following factors: the piezoelectric material parameters, the structural dimensions of the beams, the load resistance, and the input base-excitation. Unless specified otherwise, the modeling in this section assumes that the piezoelectric beams are series-connected and have a tip mass at the tip.

3.3.1. Effect of piezoelectric material parameters

The piezoelectric coefficients d_{31} and piezoelectric permittivity ε_{33} of various piezoelectric materials are different. Our attention turns to the influence of these two parameters on the energy harvesting of piezoelectric beams under a given input magnitude base-excitation.

The power FRF of the piezoelectric beams with different d_{31} and ε_{33} is shown in Fig. 10. From the graph, it is evident that when the scanning frequency matches the natural frequency of the beam, the output power will decrease monotonically with an increase in the modulus of d_{31}. However, the output power between each pair of peaks will increase as the modulus of d_{31} increases. As seen in Fig. 10(b), when the scanning frequency is lower than the first natural frequency, the change in piezoelectric permittivity ε_{33} has little impact on the output power. On the other hand, when the scanning frequency corresponds to the second and third natural frequencies, the output power increases monotonically with an increase in ε_{33}. Additionally, the influence of d_{31} and ε_{33} on the first-order natural frequency of the beam is relatively small. However, the second-order natural frequencies of the beam are positively and negatively correlated with the modulus of d_{31} and ε_{33}, respectively.

Based on the analysis above, it is clear that a comprehensive consideration of the piezoelectric coefficient and piezoelectric permittivity is necessary in order to achieve a higher output power for the piezoelectric beams. By using piezoelectric materials with a larger ε_{33} and a smaller modulus of d_{31}, a better energy harvesting effect can be achieved.

3.3.2. Effect of structural dimensions

Here we discuss the effect of the thickness of piezoelectric wafers, denoted as h_p, and base beam, denoted as h_b, on the efficiency of vibration energy harvesting. Fig. 11 shows the output voltage and tip-to-base transmissibility FRFs of the piezoelectric beams with varying thicknesses.

It can be seen from the graphs that: (i) the natural frequencies of the beam exhibit an upward trend as the piezoelectric wafer thickness h_p and the base beam thickness h_b increase, (ii) for the first two natural frequencies, the output voltage shows distinct trends of gradual increase and decrease as h_p and h_b increase, respectively, (iii) overall, the change in piezoelectric wafer thickness h_p has a more substantial impact on the natural frequency, output voltage, and tip displacement of piezoelectric beams compared to the base beam thickness h_b.

The structural dimensions of the piezoelectric cantilever beams significantly affect their energy harvesting efficiency. When determining the structural size parameters of these beams, it is important to consider not only the energy harvesting efficiency but also the cost of equipment production and the impact on the surrounding environment. While ensuring safety and staying within budget, it is crucial to optimize the effect of vibration energy harvesting as much as possible.

3.3.3. Effect of load resistance

Fig. 12 displays the output voltage, current, and power FRFs under different resistance loads. From these graphical models, it can be seen that output voltage and current of the piezoelectric beams monotonically increase and decrease along with the rise in resistance, respectively, while the change in output power is not monotonic, and there is an optimal resistance value that maximizes the output power. The resistance value corresponding to the peak output power is related to the structural and material parameters of the piezoelectric beam itself.
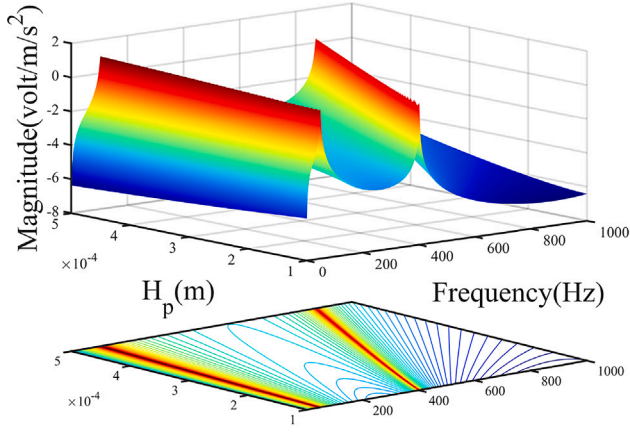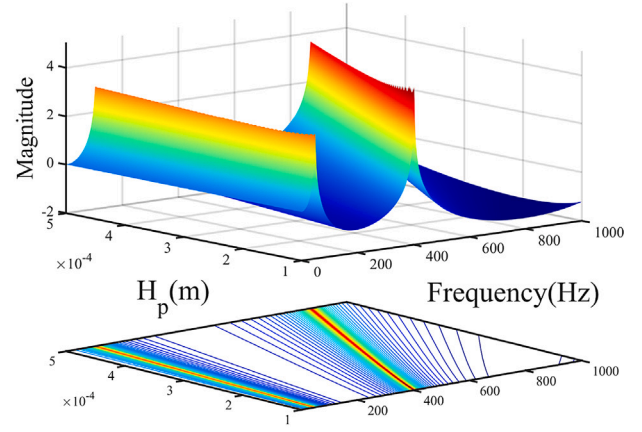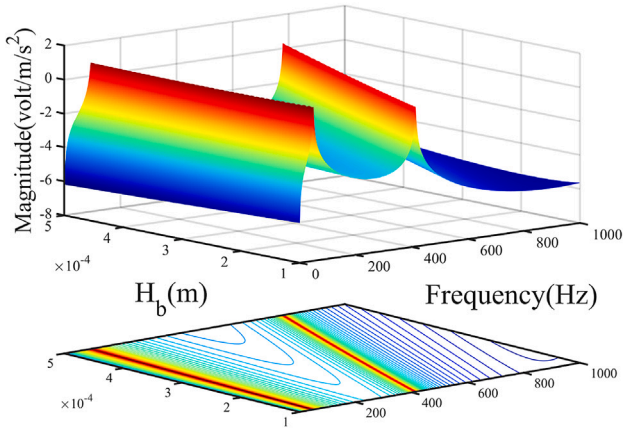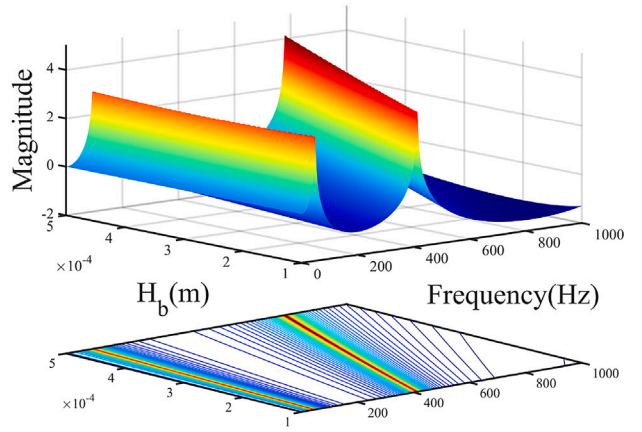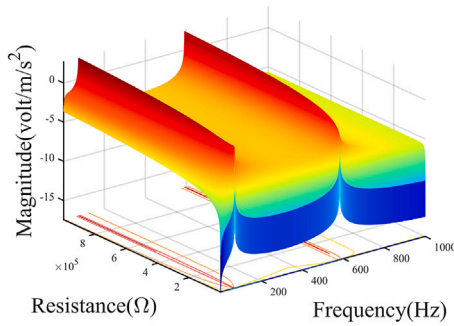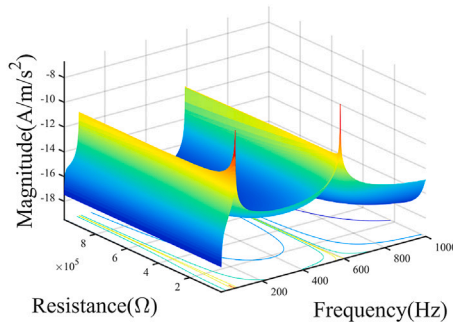
(a) Output voltage for different h_p

(b) Tip displacement for different h_p

(c) Output voltage for different h_b

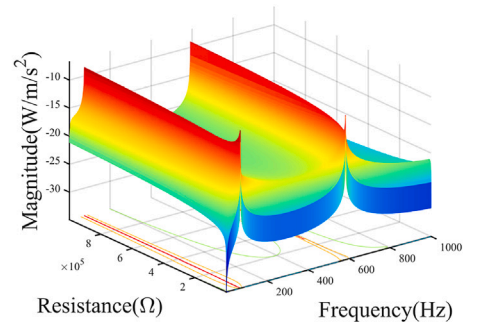**(d)** Tip displacement for different h_b

Fig. 11. Output characteristic FRFs of the piezoelectric beams with different thicknesses.

(a) Output voltage

(b) Output current

(c) Output power

Fig. 12. Output characteristic FRFs of the piezoelectric beams with different load resistances.

When these parameters change, this optimal resistance value will also change accordingly. The performance of the series-connected bimorph piezoelectric beam can be clearly understood to determine the optimal resistance for vibration energy harvesting from the results and graphs.

3.3.4. Effect of base excitation

The input base excitation, represented by the coefficient U_0 in Eq. (26b), has no impact on the structural characteristics of the piezoelectric beam. Therefore, we will only concentrate on how the base excitation affects the output characteristics of the piezoelectric beams. Fig. 13(a)
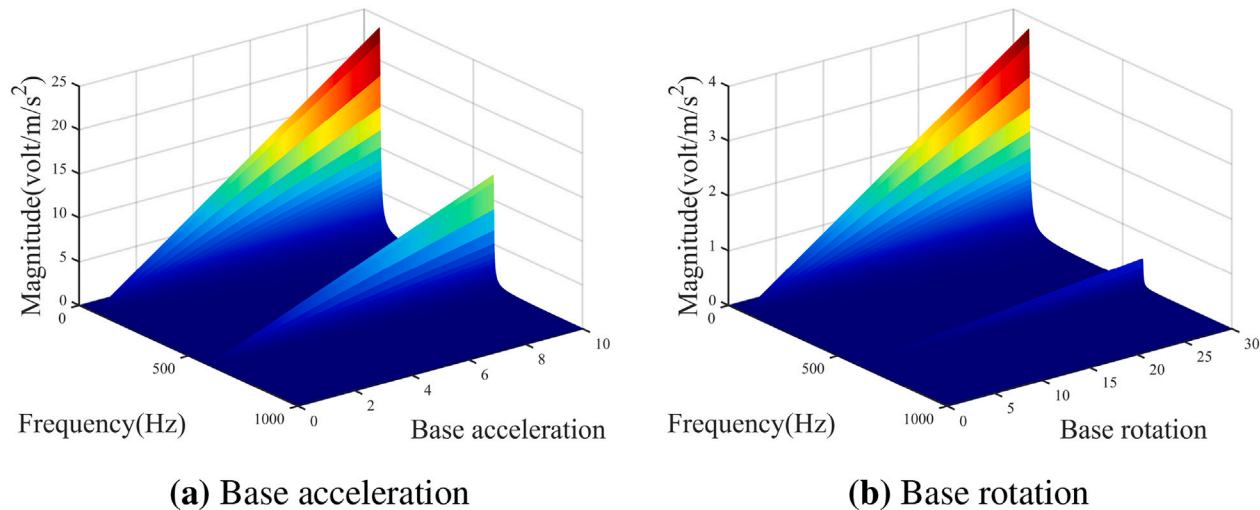
(a) Base acceleration

(b) Base rotation

Fig. 13. Output power FRF of the piezoelectric beams with different input base excitation.

and Fig. 13(b) display the output voltage FRF of the piezoelectric beam under different base acceleration and rotation excitation, respectively. It is clear that the output voltage increases linearly as the external input base acceleration changes. Similarly, an increase in external input rotation results in a linear increase in the output voltage of the beam.

4. Conclusion

This paper has developed the dynamic stiffness (DS) models for analyzing multimodal piezoelectric energy harvesting beams based on the Euler–Bernoulli beam theory and linear piezoelectric constitutive equation. The Wittrick–Williams (WW) algorithm has been employed to solve the natural frequencies of energy harvesters considering electrically-induced stiffness for the first time, which has been proven to be an exact and powerful tool for resonance frequency calculation. Additionally, both the electrically-induced stiffness and electrically-induced damping have been introduced to characterize the impact of energy harvesting circuits on the entire harvesters. The effect of different structures and parameters on the energy harvesting efficiency of the piezoelectric beams has also been analyzed. The novel contributions of this paper can be summarized as follows:

1. The DS model of piezoelectric beams based on the exact solutions of governing differential equations exhibits significantly fewer DoFs and can accurately predict the electromechanical coupling response of the beam. Moreover, as a replacement for traditional numerical modeling methods, the modeling technique has been applied to the comprehensive multimodal analysis of piezoelectric beams equipped with different tip attachments and external circuits, as well as segmented-electrode piezoelectric beams. These applications demonstrate the wide applicability and high accuracy of the proposed method in studying various piezoelectric energy harvesting scenarios.

2. The electrically-induced stiffness and electrically-induced damping are introduced to describe the impact of energy harvesting circuits on the harvesters, both of which have clear physical meaning, where the stiffness increases natural frequencies and the damping represents energy dissipation during vibration-to-electrical energy conversion. These concepts provide a clear and direct way of designing the energy harvesters.

3. As a highly efficient algorithm for accurately calculating eigenvalues, the WW algorithm has been introduced in this paper to calculate the eigenvalues of the DS matrices of piezoelectric

beams. This application of the WW algorithm enables precise frequency tuning of the piezoelectric energy harvesting structures. The natural frequency of the beam can be adjusted to match the vibration frequency of the surrounding environment to achieve the best vibration energy harvesting effect, highlighting the potential of the WW algorithm in optimizing piezoelectric energy harvesting systems for better performance in diverse environmental conditions.

4. The electromechanical coupling responses of piezoelectric beams under different structural and material parameters are analyzed using the DSM, and the influence of these factors on the energy harvesting efficiency of the beams has been discussed in this paper. This study provides a powerful tool for dynamic design and adaptive optimization of piezoelectric intelligent structures.

In summary, the proposed method can efficiently and accurately calculate the natural frequencies of the beams and predict the output characteristic frequency response of the piezoelectric beams under base excitation. Future research will focus on further considering more complex harvesting structures and nonlinear vibration energy harvesting for the design and optimization of piezoelectric energy harvesting devices. We will also establish a model of the piezoelectric intelligent structures based on high-order beam theory in the future, which will help analyze the impact of thickness stretching on the energy harvesting effect. Thus, a more comprehensive and accurate description of the mechanical and electrical behavior of the structure can be provided, and this description can serve as a powerful mathematical tool for designing piezoelectric energy harvesting structures with higher energy conversion efficiency.

CRediT authorship contribution statement

Xiang Liu: Writing – review & editing, writing – original draft, methodology, funding acquisition, and conceptualization. **Yu Wang:** Writing – review & editing, writing – original draft, visualization, and software. **Sondipon Adhikari:** Writing – review & editing. **Weixian Zhou:** Writing – review & editing.

Declaration of competing interest

The authors declare that they have no known competing financial interests or personal relationships that could have appeared to influence the work reported in this paper.
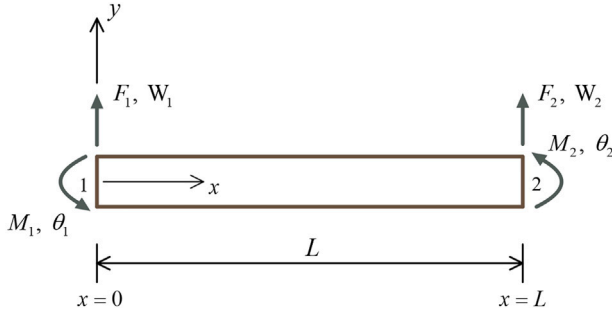
Fig. A.14. Boundary conditions for an Euler–Bernoulli beam in flexural vibration.

Appendix A

All the models presented in this paper are based on the Euler–Bernoulli beam theory, excluding axial deformations. Therefore, we only derive the DS matrix of beam's flexural deformations [83].

In Fig. A.14, the notations M, θ, F and W respectively correspond to bending moments, rotations, shear forces and displacements. The subscripts 1 and 2 will be used to represent the left and right end nodes of the beam, respectively. The deflection of the beam's cross-section at position x and time t is denoted as $w(x,t)$, and the governing differential bending motion equation of the beam is given by

$$YI\frac{\partial^4 w}{\partial x^4} + \rho A \frac{\partial^2 w}{\partial t^2} = 0 \tag{A.29}$$

where ρ and Y represent the density and Young's modulus of the material, respectively. I and A are the respectively moment of inertia and the area of beam section.

Assuming that the deflection w does a simple harmonic motion with frequency ω, so that it's given by

$$w(x,t) = W(\xi)e^{i\omega t} \tag{A.30}$$

where $\xi = x/L$ and $W(\xi)$ represents the amplitude of bending vibration. Substituting the deflection expression into the governing differential equation of the Bernoulli–Euler beam gives

$$\frac{d^4 W}{d\xi^4} - \lambda^4 W = 0, \lambda = \sqrt[4]{\frac{m\omega^2 L^4}{YI}} \tag{A.31}$$

where m represents the mass per unit length.

The solution to the above differential equation can be given

$$W(\xi) = C_1 \cos \lambda\xi + C_2 \sin \lambda\xi + C_3 \cosh \lambda\xi + C_4 \sinh \lambda\xi \tag{A.32}$$

where $C_1 - C_4$ are constants. The rotation angle, bending moment and shear force at the left end of the beam can be expressed as follows

$$\theta = \frac{1}{L}\frac{dW}{d\xi} = \frac{\lambda}{L}(-C_1 \sin \lambda\xi + C_2 \cos \lambda\xi + C_3 \sinh \lambda\xi + C_4 \cosh \lambda\xi) \tag{A.33a}$$

$$M = -\frac{YI}{L^2}\frac{d^2 W}{d\xi^2} = \frac{YI}{L^2}\lambda^2(C_1 \cos \lambda\xi + C_2 \sin \lambda\xi - C_3 \cosh \lambda\xi - C_4 \sinh \lambda\xi) \tag{A.33b}$$

$$F = \frac{YI}{L^3}\frac{d^3 W}{d\xi^3} = \frac{YI}{L^3}\lambda^3(C_1 \sin \lambda\xi - C_2 \cos \lambda\xi + C_3 \sinh \lambda\xi + C_4 \cosh \lambda\xi) \tag{A.33c}$$

Referring to Fig. A.14, the end conditions for the displacements and forces can be expressed as follows

At $x = 0$, $\quad W = W_1$, $\quad \theta = \theta_1$, $\quad F = F_{y1}$, $\quad M = M_1$ $\tag{A.34a}$

At $x = L$, $\quad W = W_2$, $\quad \theta = \theta_2$, $\quad F = -F_{y2}$, $\quad M = -M_2$ $\tag{A.34b}$

Substituting above end conditions into Eq. (A.33), the following matrices can be obtained for displacements and forces, in terms of the constants $C_1 - C_4$

$$\begin{bmatrix} W_1 \\ \theta_1 \\ W_2 \\ \theta_2 \end{bmatrix} = \begin{bmatrix} 1 & 0 & 1 & 0 \\ 0 & \lambda/L & 0 & \lambda/L \\ C_\lambda & S_\lambda & C_{h\lambda} & S_{h\lambda} \\ -\lambda S_\lambda/L & \lambda C_\lambda/L & \lambda S_{h\lambda}/L & \lambda C_{h\lambda}/L \end{bmatrix} \begin{bmatrix} C_1 \\ C_2 \\ C_3 \\ C_4 \end{bmatrix} \tag{A.35}$$

$$\begin{bmatrix} F_{y1} \\ M_1 \\ F_{y2} \\ M_2 \end{bmatrix} = \begin{bmatrix} 0 & -V_3\lambda^3 & 0 & V_3\lambda^3 \\ V_2\lambda^2 & 0 & -V_2\lambda^2 & 0 \\ -V_3\lambda^3 S_\lambda & V_3\lambda^3 C_\lambda & -V_3\lambda^3 S_{h\lambda} & -V_3\lambda^3 C_{h\lambda} \\ -V_2\lambda^2 C_\lambda & -V_2\lambda^2 S_\lambda & V_2\lambda^2 C_{h\lambda} & V_2\lambda^2 S_{h\lambda} \end{bmatrix} \begin{bmatrix} C_1 \\ C_2 \\ C_3 \\ C_4 \end{bmatrix} \tag{A.36}$$

where

$$C_\lambda = \cos \lambda, \; S_\lambda = \sin \lambda, \; C_{h\lambda} = \cosh \lambda, \; S_{h\lambda} = \sinh \lambda \tag{A.37}$$

$$V_1 = \frac{YI}{L}, \; V_2 = \frac{YI}{L^2}, \; V_3 = \frac{YI}{L^3} \tag{A.38}$$

Eliminating $C_1 - C_4$ to obtain the fourth order stiffness matrix of the beam in bending vibration

$$\begin{bmatrix} F_{y1} \\ M_1 \\ F_{y2} \\ M_2 \end{bmatrix} = \begin{bmatrix} d_1 & d_2 & d_4 & d_5 \\ d_2 & d_3 & -d_5 & d_6 \\ d_4 & -d_5 & d_1 & -d_2 \\ d_5 & d_6 & -d_2 & d_3 \end{bmatrix} \begin{bmatrix} W_1 \\ \theta_1 \\ W_2 \\ \theta_2 \end{bmatrix} \tag{A.39}$$

where

$$d_1 = \frac{W_3\lambda^3(S_\lambda C_{h\lambda} + C_\lambda S_{h\lambda})}{\Delta} \qquad d_2 = \frac{W_2\lambda^2 S_\lambda S_{h\lambda}}{\Delta} \tag{A.40a}$$

$$d_3 = \frac{W_1\lambda(S_\lambda C_{h\lambda} - C_\lambda S_{h\lambda})}{\Delta} \qquad d_4 = -\frac{W_3\lambda^3(S_\lambda + S_{h\lambda})}{\Delta} \tag{A.40b}$$

$$d_5 = \frac{W_2\lambda^2(C_{h\lambda} - C_\lambda)}{\Delta} \qquad d_6 = \frac{W_1\lambda(S_{h\lambda} - S_\lambda)}{\Delta} \tag{A.40c}$$

where $\Delta = 1 - C_\lambda C_{h\lambda}$. Eq. (A.39) can also be expressed as a simplified matrix form as shown below

$$\mathbf{f} = \mathbf{Kd} \tag{A.41}$$

where $\mathbf{f}$ and $\mathbf{d}$ are the force and displacement vector respectively, and $\mathbf{K}$ is the frequency dependent 4×4 dynamic stiffness matrix.

Appendix B

DF matrix $\mathbf{r}$ of the piezoelectric system can be obtained from the inverse matrix of DS matrix $\mathbf{K}$ as shown below [40]

$$\mathbf{r} = \mathbf{K}^{-1} = \{r_{ij}\} \tag{B.42}$$

The relationship between displacements and forces of the piezoelectric beam can be expressed by the flexibility matrix as follows:

$$\begin{bmatrix} W_0 \\ \theta_0 \\ W_L \\ \theta_L \end{bmatrix} = \begin{bmatrix} r_{11} & r_{12} & r_{13} & r_{14} \\ r_{21} & r_{22} & r_{23} & r_{24} \\ r_{31} & r_{32} & r_{33} & r_{34} \\ r_{41} & r_{42} & r_{43} & r_{44} \end{bmatrix} \begin{bmatrix} F_0 \\ M_0 \\ F_L \\ M_L \end{bmatrix} \tag{B.43}$$

where r_{ij} represents the element in the Row i and Column j of DF matrix $\mathbf{r}$. By setting F_L and M_L to zero and eliminating F_0 and M_0, one can

express the tip displacement W_L and rotation θ_L in terms of W_0 and θ_0 as follows

$$\begin{bmatrix} W_L \\ \theta_L \end{bmatrix} = \frac{1}{r_{11}r_{22} - r_{21}r_{12}} \begin{bmatrix} r_{31}r_{22} - r_{32}r_{21} & -r_{31}r_{12} + r_{32}r_{11} \\ r_{41}r_{22} - r_{42}r_{21} & -r_{41}r_{12} + r_{42}r_{11} \end{bmatrix} \begin{bmatrix} W_0 \\ \theta_0 \end{bmatrix}$$
(B.44)

Then, the voltage and displacement of the piezoelectric beam can be expressed in terms of W_0 and θ_0 as

$$V = G\left[\left(r_{41}r_{22} - r_{42}r_{21}\right)/\gamma\right] W_0 + G\left[\left(-r_{41}r_{12} + r_{42}r_{11} - \gamma\right)/\gamma\right]\theta_0 \quad \text{(B.45a)}$$

$$W_L = \left[\left(r_{31}r_{22} - r_{32}r_{21}\right)/\gamma\right] U_0 + \left[\left(-r_{31}r_{12} + r_{32}r_{11}\right)/\gamma\right]\theta_0 \quad \text{(B.45b)}$$

where $\gamma = r_{11}r_{22} - r_{12}r_{21}$.

Data availability

Data will be made available on request.

References

[1] Challa VR, Prasad M, Fisher FT. Towards an autonomous self-tuning vibration energy harvesting device for wireless sensor network applications. Smart Mater Struct 2011;20(2):025004.

[2] Le MQ, Capsal J-F, Lallart M, Hebrard Y, Van Der Ham A, Reffe N, et al. Review on energy harvesting for structural health monitoring in aeronautical applications. Prog Aerosp Sci 2015;79:147–57.

[3] Wahbah M, Alhawari M, Mohammad B, Saleh H, Ismail M. Characterization of human body-based thermal and vibration energy harvesting for wearable devices. IEEE J Emerg Sel Top Circuits Syst 2014;4(3):354–63.

[4] Cadei A, Dionisi A, Sardini E, Serpelloni M. Kinetic and thermal energy harvesters for implantable medical devices and biomedical autonomous sensors. Meas Sci Technol 2013;25(1):012003.

[5] Saadon S, Sidek O. A review of vibration-based mems piezoelectric energy harvesters. Energy Convers Manag 2011;52(1):500–04.

[6] Azizi S, Ghodsi A, Jafari H, Ghazavi MR. A conceptual study on the dynamics of a piezoelectric mems (micro electro mechanical system) energy harvester. Energy 2016;96:495–506.

[7] Crovetto A, Wang F, Hansen O. Modeling and optimization of an electrostatic energy harvesting device. J Microelectromech Syst 2014;23(5):1141–55.

[8] Khan FU, Qadir MU. State-of-the-art in vibration-based electrostatic energy harvesting. J Micromech Microeng 2016;26(10):103001.

[9] Carneiro P, dos Santos MPS, Rodrigues A, Ferreira JA, Simões JA, Marques AT, et al. Electromagnetic energy harvesting using magnetic levitation architectures: a review. Appl Energy 2020;260:114191.

[10] Costanzo A, Dionigi M, Masotti D, Mongiardo M, Monti G, Tarricone L, et al. Electromagnetic energy harvesting and wireless power transmission: a unified approach. Proc IEEE 2014;102(11):1692–711.

[11] Friswell MI, Ali SF, Bilgen O, Adhikari S, Lees AW, Litak G. Non-linear piezoelectric vibration energy harvesting from a vertical cantilever beam with tip mass. J Intell Mater Syst Struct 2012;23(13):1505–21.

[12] Kim HS, Kim J-H, Kim J. A review of piezoelectric energy harvesting based on vibration. Int J Precis Eng Manuf 2011;12:1129–41.

[13] Wu N, Bao B, Wang Q. Review on engineering structural designs for efficient piezoelectric energy harvesting to obtain high power output. Eng Struct 2021;235:112068.

[14] Fang Z-W, Zhang Y-W, Li X, Ding H, Chen L-Q. Integration of a nonlinear energy sink and a giant magnetostrictive energy harvester. J Sound Vib 2017;391:35–49.

[15] Mohammadi S, Esfandiari A. Magnetostrictive vibration energy harvesting using strain energy method. Energy 2015;81:519–25.

[16] Yang J, Chen J, Yang Y, Zhang H, Yang W, Bai P, et al. Broadband vibrational energy harvesting based on a triboelectric nanogenerator. Adv Energy Mater 2014;4(6):1301322.

[17] Chen J, Wang ZL. Reviving vibration energy harvesting and self-powered sensing by a triboelectric nanogenerator. Joule 2017;1(3):480–521.

[18] Xiao X, Zhang X, Wang S, Ouyang H, Chen P, Song L, et al. Honeycomb structure inspired triboelectric nanogenerator for highly effective vibration energy harvesting and self-powered engine condition monitoring. Adv Energy Mater 2019;9(40):1902460.

[19] Abdehvand MZ, Roknizadeh SAS, Mohammad-Sedighi H. Modeling and analysis of novel coupled magneto-electro-aeroelastic continuous system for flutter-based energy harvesting system. Energy 2021;230:120742.

[20] Cong M, Gao Y, Wang W, He L, Mao X, Long Y, et al. A broadband hybrid energy harvester with displacement amplification decoupling structure for ultra-low vibration energy harvesting. Energy 2024;290:130089.

[21] Nabavi S, Zhang L. T-shaped piezoelectric structure for high-performance mems vibration energy harvesting. J Microelectromech Syst 2019;28(6):1100–12.

[22] Xie Z, Wang T, Kwuimy CK, Shao Y, Huang W. Design, analysis and experimental study of a t-shaped piezoelectric energy harvester with internal resonance. Smart Mater Struct 2019;28(8):085027.

[23] Nabavi S, Aljaroudi A, Zhang L. T-shaped piezoelectric vibratory mems harvester with integration of highly efficient power management system. In: Journal of Physics: Conference Series; Vol. 1052. IOP Publishing; 2018. p. 012102.

[24] Nie X, Tan T, Yan Z, Yan Z, Hajj MR. Broadband and high-efficient l-shaped piezoelectric energy harvester based on internal resonance. Int J Mech Sci 2019;159:287–305.

[25] Yao M, Liu P, Ma L, Wang H, Zhang W. Experimental study on broadband bistable energy harvester with l-shaped piezoelectric cantilever beam. Acta Mech Sin 2020;36:557–77.

[26] Liu D, Al-Haik M, Zakaria M, Hajj MR. Piezoelectric energy harvesting using l-shaped structures. J Intell Mater Syst Struct 2018;29(6):1206–15.

[27] Xie X, Carpinteri A, Wang Q. A theoretical model for a piezoelectric energy harvester with a tapered shape. Eng Struct 2017;144:19–25.

[28] Keshmiri A, Wu N, Wang Q. A new nonlinearly tapered fgm piezoelectric energy harvester. Eng Struct 2018;173:52–60.

[29] Zhao X, Shang Z, Luo G, Deng L. A vibration energy harvester using aln piezoelectric cantilever array. Microelectron Eng 2015;142:47–51.

[30] Na Y, Lee M-S, Lee JW, Jeong YH. Wind energy harvesting from a magnetically coupled piezoelectric bimorph cantilever array based on a dynamic magneto-piezoelastic structure. Appl Energy 2020;264:114710.

[31] Mažeika D, Čeponis A, Yang Y, et al. Multifrequency piezoelectric energy harvester based on polygon-shaped cantilever array. Shock Vib 2018;2018.

[32] Wang G, Liao W-H, Yang B, Wang X, Xu W, Li X. Dynamic and energetic characteristics of a bistable piezoelectric vibration energy harvester with an elastic magnifier. Mech Syst Signal Process 2018;105:427–46.

[33] Vijayan K, Friswell M, Khodaparast HH, Adhikari S. Non-linear energy harvesting from coupled impacting beams. Int J Mech Sci 2015;96:101–09.

[34] Poya R, Gil AJ, Ledger PD. A computational framework for the analysis of linear piezoelectric beams using hp-fem. Comput Struct 2015;152:155–72.

[35] Leadenham S, Erturk A. Unified nonlinear electroelastic dynamics of a bimorph piezoelectric cantilever for energy harvesting, sensing, and actuation. Nonlinear Dyn 2015;79:1727–43.

[36] Hosseini R, Nouri M. Shape design optimization of unimorph piezoelectric cantilever energy harvester. J Comput Appl Mech 2016;47(2):247–59.

[37] Guo L, Wang H. Multi-physics modeling of piezoelectric energy harvesters from vibrations for improved cantilever designs. Energy 2023;263:125870.

[38] Ghodsi M, Ziaiefar H, Mohammadzaheri M, Al-Yahmedi A. Modeling and characterization of permendur cantilever beam for energy harvesting. Energy 2019;176:561–69.

[39] Banerjee S, Roy S. A dimensionally reduced order piezoelectric energy harvester model. Energy 2018;148:112–22.

[40] Bonello P, Rafique S. Modeling and analysis of piezoelectric energy harvesting beams using the dynamic stiffness and analytical modal analysis methods. 2011.

[41] Umeda M, Nakamura K, Ueha S. Analysis of the transformation of mechanical impact energy to electric energy using piezoelectric vibrator. Jpn J Appl Phys 1996;35(5S):3267.

[42] Umeda M, Nakamura K, Ueha S. Energy storage characteristics of a piezo-generator using impact induced vibration. Jpn J Appl Phys 1997;36(5S):3146.

[43] Cho YS, Pak YE, Han CS, Ha SK. Five-port equivalent electric circuit of piezoelectric bimorph beam. Sens Actuators A Phys 2000;84(1–2) 140–48.

[44] Ha SK. Analysis of the asymmetric triple-layered piezoelectric bimorph using equivalent circuit models. J Acoust Soc Am 2001;110(2):856–64.

[45] Guan M, Liao W-H. Studies on the circuit models of piezoelectric ceramics. In: International Conference on Information Acquisition, 2004. Proceedings; IEEE; 2004. p. 26–31.

[46] Elvin NG, Elvin AA. A general equivalent circuit model for piezoelectric generators. J Intell Mater Syst Struct 2009;20(1):3–9.

[47] Elvin NG, Elvin AA. A coupled finite element—circuit simulation model for analyzing piezoelectric energy generators. J Intell Mater Syst Struct 2009;20(5):587–95.

[48] Yang Y, Tang L. Equivalent circuit modeling of piezoelectric energy harvesters. J Intell Mater Syst Struct 2009;20(18):2223–35.

[49] Williams C, Yates RB. Analysis of a micro-electric generator for microsystems. Sens Actuators A Phys 1996;52(1–3) 8–11.

[50] Baishya S, Borthakur D, Kashyap R, Chatterjee A. A high precision lumped parameter model for piezoelectric energy harvesters. IEEE Sens J 2017;17(24):8350–55.

[51] Wang G-Q, Lu Y-M, et al. An improved lumped parameter model for a piezoelectric energy harvester in transverse vibration. Shock Vib 2014;2014.

[52] Wang J, Li G, Zhang M, Zhao G, Jin Z, Xu K, et al. Energy harvesting from flow-induced vibration: a lumped parameter model, energy sources, part A: recovery. Util Environ Eff 2018;40(24):2903–13.

[53] Weinberg MS. Working equations for piezoelectric actuators and sensors. J Microelectromech Syst 1999;8(4):529–33.

[54] Roundy S, Wright PK, Rabaey J. A study of low level vibrations as a power source for wireless sensor nodes. Comput Commun 2003;26(11):1131–44.

[55] Dutoit NE, Wardle BL, Kim S-G. Design considerations for mems-scale piezoelectric mechanical vibration energy harvesters. Integr Ferroelectr 2005;71(1):121–60.

[56] Erturk A, Inman DJ. Issues in mathematical modeling of piezoelectric energy harvesters. Smart Mater Struct 2008;17(6):065016.

[57] Erturk A. Assumed-modes modeling of piezoelectric energy harvesters: Euler–bernoulli, rayleigh, and timoshenko models with axial deformations. Comput Struct 2012;106:214–47.

[58] Wang S. A finite element model for the static and dynamic analysis of a piezoelectric bimorph. Int J Solids Struct 2004;41(15):4075–96.

[59] Thein CK, Ooi BL, Liu J-S, Gilbert JM. Modelling and optimisation of a bimorph piezoelectric cantilever beam in an energy harvesting application. J Eng Sci Technol 2016;11(2):212–27.

[60] Roundy SJ. Energy scavenging for wireless sensor nodes with a focus on vibration to electricity conversion. Berkeley: University of California; 2003.

[61] Givois A, Deü J-F, Thomas O. Dynamics of piezoelectric structures with geometric nonlinearities: a non-intrusive reduced order modelling strategy. Comput Struct 2021;253:106575.

[62] Kalkowski MK, Rustighi E, Waters TP. Modelling piezoelectric excitation in waveguides using the semi-analytical finite element method. Comput Struct 2016;173:174–86.

[63] Matos A, Guedes J, Jayachandran K, Rodrigues H. Computational model for power optimization of piezoelectric vibration energy harvesters with material homogenization. Comput Struct 2017;192:144–56.

[64] Fattahi I, Mirdamadi HR. Novel composite finite element model for piezoelectric energy harvesters based on 3d beam kinematics. Compos Struct 2017;179:161–71.

[65] Erturk A, Inman DJ. A distributed parameter electromechanical model for cantilevered piezoelectric energy harvesters. J Vib Acoust 2008;130(4).

[66] Erturk A. Electromechanical modeling of piezoelectric energy harvesters. Ph.D. thesis. Virginia Tech; 2009.

[67] Erturk A, Renno JM, Inman DJ. Modeling of piezoelectric energy harvesting from an l-shaped beam-mass structure with an application to uavs. J Intell Mater Syst Struct 2009;20(5):529–44.

[68] Abdelkefi A, Nayfeh AH, Hajj MR. Global nonlinear distributed-parameter model of parametrically excited piezoelectric energy harvesters. Nonlinear Dyn 2012;67:1147–60.

[69] Carrera E, Zappino E, Li G. Analysis of beams with piezo-patches by node-dependent kinematic finite element method models. J Intell Mater Syst Struct 2018;29(7):1379–93.

[70] Zappino E, Li G, Carrera E. Node-dependent kinematic elements for the dynamic analysis of beams with piezo-patches. J Intell Mater Syst Struct 2018;29(16):3333–45.

[71] Bonello P, Groves K. Vibration control using a beam-like adaptive tuned vibration absorber with an actuator-incorporated mass element, Proc Inst Mech Eng Part C J Mech Eng Sci 2009;223(7):1555–67.

[72] Hafeez MB, Krawczuk M. A review: applications of the spectral finite element method. Arch Comput Methods Eng 2023;30(5):3453–65.

[73] Lee U. Spectral element method in structural dynamics. John Wiley and Sons; 2009.

[74] Machado MR, Fabro AT, de Moura BB. Spectral element approach for flexural waves control in smart material beam with single and multiple resonant impedance shunt circuit. J Comput Nonlinear Dyn 2020;15(12):121003.

[75] Park HW, Kim EJ, Lim KL, Sohn H. Spectral element formulation for dynamic analysis of a coupled piezoelectric wafer and beam system. Comput Struct 2010;88:9–10) 567–80.

[76] Liu X, Sun C, Banerjee JR, Dan H-C, Chang L. An exact dynamic stiffness method for multibody systems consisting of beams and rigid-bodies. Mech Syst Signal Process 2021;150:107264.

[77] Liu X, Zhao Y, Zhou W, Banerjee JR. Dynamic stiffness method for exact longitudinal free vibration of rods and trusses using simple and advanced theories. Appl Math Model 2022;104:401–20.

[78] Liu X, Liu X, Adhikari S, Yin S. Extended wittrick–williams algorithm for eigenvalue solution of stochastic dynamic stiffness method. Mech Syst Signal Process 2022;166:108354.

[79] Liu X, Lu Z, Adhikari S, Li Y, Banerjee JR. Exact wave propagation analysis of lattice structures based on the dynamic stiffness method and the wittrick–williams algorithm. Mech Syst Signal Process 2022;174:109044.

[80] Liu X, Pagani A, Carrera E, Liu X. Free vibration analysis of composite beams and laminated reinforced panels by refined dynamic stiffness method and cuf-based component-wise theory. Compos Struct 2024;337:118058.

[81] Odegard GM. Constitutive modeling of piezoelectric polymer composites. Acta Mater 2004;52(18):5315–30.

[82] Wittrick W, Williams F. A general algorithm for computing natural frequencies of elastic structures. Q J Mech Appl Math 1971;24(3):263–84.

[83] Banerjee J. Dynamic stiffness formulation for structural elements: a general approach. Comput Struct 1997;63(1):101–03.